Alma Mater Studiorum · Università di Bologna

Scuola di Scienze
Dipartimento di Fisica e Astronomia
Corso di Laurea in Fisica

Modeling the Cosmic-Ray proton flux on low Earth orbit space telescopes: study of the accuracy with respect to in-flight measurements

Relatore:
Prof. Gabriele Giovannini

Correlatrice:
Dott.ssa Valentina Fioretti

Presentata da:
Matteo Fonsetti

Sessione IV
Anno Accademico 2019/2020

This Bachelor Thesis has been carried out
at the INAF OAS Bologna as part of the
institute's research activities

Qualsiasi via é solo una via, e non c'é nessun affronto, a se stessi o agli altri, nell'abbandonarla, se questo é ció che il tuo cuore ti dice di fare... Esamina ogni via con accuratezza e ponderazione. Provala tutte le volte che lo ritieni necessario. Quindi poni a te stesso, e a te stesso soltanto, una domanda... Questa via ha un cuore? Se lo ha, la via é buona. Se non lo ha, non serve a niente.

Carlos Castaneda, The Teachings of Don Juan

Contents

Abstract

L'avvento dell'era spaziale ha consentito alla civiltá umana di fare notevoli passi avanti nello studio dei fenomeni celesti. I grandi telescopi di terra, fino a qualche decennio fa uniche porte a nostra disposizione per studiare nebulose, stelle e galassie, sono oggi affiancati da altrettanto sofisticati telescopi spaziali in grado di operare oltre l'atmosfera terrestre in un ambiente estremo e fortemente proibitivo. Tale ambiente é pervaso da flussi di particelle, i raggi cosmici, che si estendono per oltre 20 ordini di grandezza in energia, ed é costantemente spazzato dagli intensi venti provenienti dal Sole. Quando i raggi cosmici interagiscono con il campo magnetico terrestre, con l'atmosfera o con i venti solari, danno luogo a complessi fenomeni che, da un lato, rappresentano un banco di prova prezioso per l'astrofisica delle particelle, dall'altro costituiscono una fonte di disturbo per le missioni di osservazione X e gamma poiché interagiscono con la strumentazione di bordo incrementando il cosiddetto rumore di fondo strumentale. Appare allora evidente quanto una conoscenza il piú possibile dettagliata di come stimare (e prevedere) tale rumore di fondo sia sempre piú necessaria per la buona riuscita di una missione spaziale. In questo lavoro di tesi mi sono focalizzato sullo studio del modello che rappresenta l'attuale stato dell'arte nella modellizzazione del flusso di protoni di raggi cosmici in orbita bassa; dopo una presentazione preliminare di tale modello, l'ho messo all'opera confrontandone le previsioni con i dati ottenuti dall'esperimento AMS-01, montato sullo Space Shuttle Discovery e lanciato da Cape Kennedy nel 1998, e dagli esperimenti da pallone BESS, IMAX e CAPRICE, le cui prese dati hanno avuto luogo sopra il lago Manitoba, in Canada. Lo scopo del lavoro é stato valutare la precisione del modello rispetto alle misure. Riguardo ad AMS-01, le discrepanze ottenute si sono attestate attorno ad un 10% circa per i bin a piú alta energia dello spettro, quelli cioé dominati dalla power law, e su percentuali fino a 30 volte maggiori nella regione di cutoff, a piú bassa energia; occorre

tuttavia segnalare come, nel secondo caso, i flussi in gioco siano molto bassi e quindi le incertezze relative meno influenti nel computo totale del flusso di protoni. Un comportamento analogo ma meno marcato é stato registrato per gli esperimenti da pallone, in merito ai quali le discrepanze si sono attestate attorno al 10% per BESS, attorno al 30% per IMAX e attorno al 10% con un picco massimo nella regione di cutoff di $\sim$25% per CAPRICE. In generale, per tutti gli esperimenti considerati si é registrato un posizionamento dei dati al di sotto delle previsioni medie del modello, un possibile indizio di una loro potenziale leggera sovrastima. Quanto ottenuto per AMS-01 é stato infine rielaborato allo scopo di effettuare una stima del flusso di protoni primari a cui sará sottoposta una missione operante in orbita bassa nellâimmediato futuro. La scelta é ricaduta sulla missione XRISM, il cui lancio é previsto per gennaio 2022; per la mia analisi ho considerato come finestra temporale il periodo nominale di lancio e come latitudine geomagnetica la regione equatoriale. Come risultato si sono ottenute tre stime, corrispondenti a tre differenti approcci in riferimento agli errori sul flusso adottati: il "peggior scenario possibile", uno scenario piú realistico, e uno scenario mediato fra i due precedenti.

Abstract

The coming of the Space Age allowed humankind to achieve outstanding results in the study of celestial phenomena. Large ground-based telescopes, until a few decades ago the only doors at our disposal to study nebulae, stars and galaxies, are today flanked by equally sophisticated spaceborne telescopes capable of operating beyond the Earth's atmosphere in an extreme and highly prohibitive environment. This environment is filled by cosmic rays, streams of particles extending over 20 orders of magnitude in energy, and is constantly swept by the intense winds propagating from the Sun. When cosmic rays interact with the Earth's magnetic field, with the atmosphere or with solar winds, they give rise to complex phenomena which, on the one hand, represent a valuable experimental work bench for particle astrophysics and, on the other, constitute a source of disturbance for X and gamma missions since, by interacting with the on-board instrumentation, they may increase the so-called instrumental background noise. It is therefore clear that, having as much in-depth knowledge as possible in estimating and predicting such background noise, represents a milestone for the success of a space mission. In this dissertation I focused on studying the algorithm that represents the current state of the art in modeling the cosmic rays' primary protons component in low Earth orbit; after an introduction of the model itself, I put it to work by comparing its predictions with the data obtained by the AMS-01 experiment, which was installed on the Space Shuttle Discovery and launched from Cape Kennedy in 1998, and by the BESS, IMAX and CAPRICE balloon-borne experiments whose data was taken over Lake Manitoba, Canada. The aim of this work is to study the accuracy of the model itself by comparing its previsions with the actual data obtained by the experiments. With regard to AMS-01, the obtained discrepancies set around 10% for the higher energy bins of the spectrum, i.e. those dominated by the power law, and on percentages up to 30 times

greater in the lower energy cutoff region; it should however be noted that, for the latter, the fluxes involved are very low and, therefore, the relative uncertainties are less influential in the flux's total outcome. A similar but less pronounced behavior was observed for the balloon-borne experiments, with respect to which discrepancies set around 10% for BESS, 30% for IMAX and 10% for CAPRICE, with a peak inside the cutoff region of $\sim$25% for the latter. In general, for all the considered experiments a positioning of the data below the average predictions of the model was observed, a clue which may indicate a potential slight overestimation. The results obtained for AMS-01 were finally reworked in order to estimate the primary protons' flux to which a near future low Earth orbit mission may be subjected. The choice fell on the XRISM space mission, whose launch is scheduled for January 2022; for my analysis the equatorial region as geomagnetic latitude and the nominal launch period as time window have been considered. As a result, three estimates were obtained corresponding to three different approaches in reference to the flux's errors adopted: the "worst possible scenario", a more realistic scenario, and a scenario mediated between the two previous ones.

Chapter 1

Introduction

Our knowledge and appreciation of the laws governing the Universe has increased over the last four decades due to orbiting space telescopes since they allow us to obtain clearer observations thanks to the absence of twinkling distortion, glow from the sky or light pollution.
The environment where these telescopes operate is a dynamic and complex system in which particles of all types flow almost to the speed of light, accelerated and deflected by the intense electromagnetic field generated by our planet and by the strong solar wind propagating from the Sun. Such streams of highly energetic particles contribute to the so called instrument background noise which must be taken into account in order to predict/avoid interferences and, therefore, conduct the experiments in the best accurate way possible; a canvas of models able to reproduce in detail the radiation environment surrounding the telescope, which also depends on the operational orbit, is therefore needed.
The aim of this work is to study the state of the art in terms of models and data currently available for the evaluation of the primary proton flux in low Earth orbit (LEO) in order to provide an estimation of the accuracy of these models compared to the actual data obtained by the experiments.
The operational work bench, the low Earth orbit, will be discussed in the next two sections, section 1.1, where a brief illustration of the LEO's benefits

and disadvantages will be given, and section 1.2, where I will introduce the LEO environment in terms of its constituents.
I will then focus on the Galactic Cosmic Rays (GCR), presenting their composition, their interaction with the Earth's magnetic field and the GCR proton model in LEO (Chapter 2).
Chapter 3 presents the comparison of the proton model with data taken by the AMS 01 LEO mission and the BESS, IMAX and CAPRICE balloon-borne experiments.
An estimate of the primary protons' flux for a near future low Earth mission, the X-ray Imaging and Spectroscopy Mission (XRISM), which is expected to launch in 2022, is finally carried out in Chapter 4.
Conclusions will be given in chapter 5.

1.1 The low Earth orbit

We define as low Earth orbit (LEO) an orbit extending in an altitude between 160 and 2000 kilometers, relatively close to the Earth's surface.
In order to maintain a steady LEO orbit, satellites need a mean velocity of about 7.8 km/s (28000 km/h) which reduces with the increasing of the altitude and a delta-v (atmospheric and gravity drag corrections included) starting around 9.4 km/s.
The orbital period, that is the time needed to orbit the Earth once, may vary between 88 to 127 minutes [1].
In the history of space exploration, the vast majority of human missions have taken and still take place in low Earth orbit; this comes from a wide range of reasons which result to be of great benefit for space applications:

- great versatility, as the LEO satellites' orbital plane can be tilted, dramatically increasing the available routes that can be adopted;
- lower costs compared to higher altitudes' orbits, due to the fact that the

[1] https://www.universetoday.com/85322/what-is-low-earth-orbit/

deployment of rockets and space vehicles beyond 1000 kilometers would require significantly more fuel for the insertion's orbital maneuvers;

- high bandwidth and low communication time lag (latency) thanks to the closer proximity to Earth. This makes LEO the best choice for Earth observation satellites, also because the rapid orbital period allows the view of the same region on the surface multiple times in a single day;

- lower radiation doses at which the orbiting vehicles are exposed, thanks to the shielding effect provided by the Earth's magnetic field, which will be described more in detail in section 2.2. This allows both engineering and scientific advantages, such as the reduction of shielding requirements by spacecrafts – hence less weight and less costs – and a lower background noise in the observation of the high energy universe. The latter makes LEO the perfect place for most scientific satellites in the form of X and γ-ray telescopes.

In a nutshell, LEO represents the simplest, cheapest and safest location for the deployment of satellites, space stations, and crewed space missions; on the other side, LEO presents also some disadvantages which must be taken into account:

- the Earth shields a large portion of the sky (about 30% for an altitude of 550 km) hence reducing the field of view of astronomical space telescopes;

- an atmospherics' drag from gases in the thermosphere or exosphere is present, causing a slight and constant orbital decay which requires periodic reboosting to maintain the orbital stability or, sometimes, the launch of replacement satellites when old ones re-enter;

- the presence of space debris, in the form of discarded rocket stages, non-functioning satellites and volatile particles, the latter produced by

stages ignitions and by the satellites' corrosion induced by high energy radiation and atmospheric atoms, ions, and free radicals, most notably atomic oxygen.

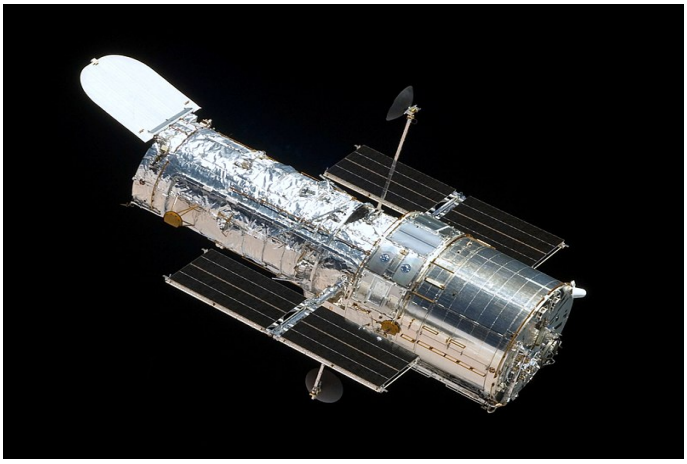

Figure 1.1: The Hubble Space Telescope, the most known space telescope working in low Earth orbit. Image taken by the departing Space Shuttle Atlantis, mission 4 (STS-125), 2009.

1.2 The LEO environment

The LEO's radiation environment consists of a wide multiplicity of components which will be now briefly described; these components contribute to the so called "instrumental background" of high energy telescopes, i.e. the count rate generated by particles interacting with the spacecraft material outside the field of view and reducing the performance of the mission; on the other hand, the particles populating the LEO regions give important insights on the Earth's magnetic field and the Sun's activity.
The main components of the LEO space environment can be summarized as follows:

- the diffuse photonic background, a nearly isotropic emission of X and γ-ray radiation extending from below 1 keV up to hundreds of MeVs. The X-ray background, except at very low energies where it arises from hot plasma in the Local Hot Bubble, the Galactic Disk and the Galactic Halo (Lumb et al. 2002), has extragalactic origin and it generates

from unresolved Active Galactic Nuclei integrated over cosmic time. The γ-ray component is the sum of a galactic emission, given by the interaction of cosmic rays with the interstellar medium, and the extra-galactic contribution of blazars, star-forming and radio galaxies, and diffuse emission (Ajello et al. 2015 [1]).

- the Cosmic Rays (CR, see Sect. 2.1), composed of high energy nuclei propagating from outer space and mainly of galactic origin.
  The Galactic Cosmic Rays (GCR) approximately consist of 98% nuclei of which 87% Hydrogen, 12% Helium, 1% heavier nuclei (Simpson (1983)), and 2% leptons (>90%, Adriani et al. (2009)), covering an energy range which extends from a few MeV up to $> 10^{15}$ eV (Smart and Shea, 1985).
  The intensity of primary nucleons in the energy range from several GeV to beyond 100 TeV is given approximately by

$$I_N(E) \approx 1.8 \times 10^4 (E/1GeV)^{-\alpha} \qquad \frac{nucleons}{m^2\ s\ sr\ GeV} \tag{1.1}$$

  where E is the energy per nucleon (rest mass energy included) and $\alpha \equiv \gamma+1 = 2.7$ is the differential spectral index of the CR's flux, with γ representing the integral spectral index (Patrignani, 2017).
  The electrons' spectrum in the range between 100 MeV to 5 GeV is dependent by the Jovian's 10 hours rotation period, showing a 13-month "seasonal", a peculiarity which depends by the relative position between the Earth and Jupiter (Smart and Shea, 1985).
  The maximum propagation of the electrons between the Jovian's magnetosphere and the Earth takes place when the interplanetary magnetic field lines passing near the Earth connects to the Jovian magnetosphere, an event which occurs approximately once every 13 months; during this period, called "electron season", peaks in electron fluxes which may last for several months are observed.
  It must be noted, however, that such propagation is quite variable, depending on the status of the interplanetary medium.

In general, the intensity of cosmic rays depends on the solar activity – hence by the inverse of its sunspot number – increasing during minimum and decreasing during maximum.

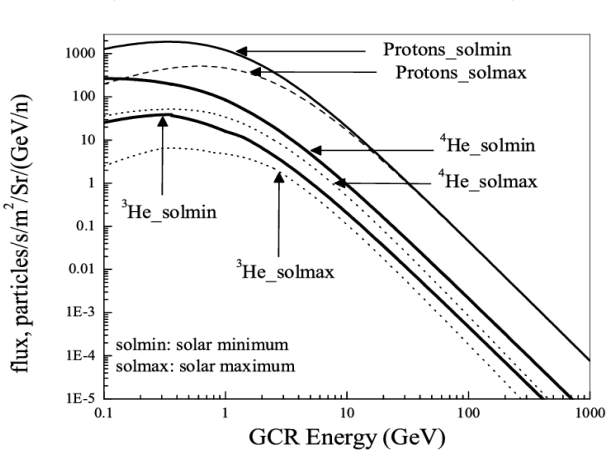

Figure 1.2: Differential spectra for CR protons and He nuclei.
For each species, the upper and lower curves indicate the solar minimum and the solar maximum spectrum, respectively. [2].

A more in-depth of the protons composing the GCRs is given in Chapter 2;

- albedo particles, i.e. a class of low energy particles (mainly protons, leptons, neutrons and photons) generated by both GCRs interacting with the atmosphere and the reflection of cosmic photonic radiation. When the primary cosmic ray component mentioned above interacts with air nuclei in the atmosphere a large cascade of lighter particles is produced, above all pions and kaons, which later decade to produce muons. A small fraction of this secondary radiation, mainly hadrons, leptons, photons and neutrons, will escape the atmosphere and contribute to the total radiation flux exposure to Earth orbiting satellites.

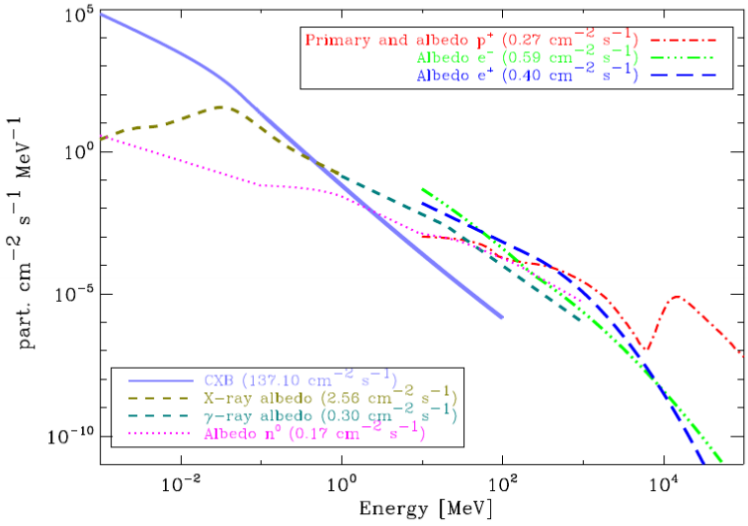

Figure 1.3: The space radiation environment in LEO for an altitude of 550 km and a geomagnetic latitude $< 5°$ [3].

Chapter 2

The model for GCR protons in low Earth orbit

2.1 Galactic cosmic rays

Cosmic rays (CR) consist of high-energy nuclei believed to propagate throughout all space at nearly the speed of light of both galactic and, at very high energies, of extragalactic origin.
Entering the Solar System, the GCRs' flux undergoes two different types of modulation:

- solar modulation: it consists of an energy loss due to diffusional, convectional and adiabatic interactions with the solar wind, deeply tied to the Sun's magnetic activity, hence to its $\sim$ 11-year sunspot cycle.
  According to extensive studies covering a period between 50s to 90s, the length of a solar cycle may vary in a 9 to 13 years range, with an average value of 11.5 years (Stassinopoulos et al. 1996); it was later discovered that this period can be divided itself in 2 subperiods directly dependent on the number of sunspots appearing on the Sun's surface: a maximum phase and a relatively quite minimum phase, lasting 7 and 4 years respectively (Barth, 1997).
  The effect of our star's activity results in a more or less strong solar

wind, which streams out from the Sun's corona and creates the so called Interplanetary Magnetic Field (IMF). The result is a variable modulation on the GCRs' flux strictly dependent by the solar phase, stronger on a maximum and lighter on a minimum, summarized by the solar modulation parameter ϕ, expressed in megavolts (MV).
By multiplying it by Ze, with Z the atomic number of the particle and e the magnitude of the electron charge, the solar parameter ϕ becomes the potential energy loss by the particle while moving from the solar boundary to the Earth. Being ϕ so deeply linked to the Sun's activity, its value may vary in a range between $\sim$ 300 to $\sim$ 1500 MV [4], decreasing during minimum and increasing during maximum.

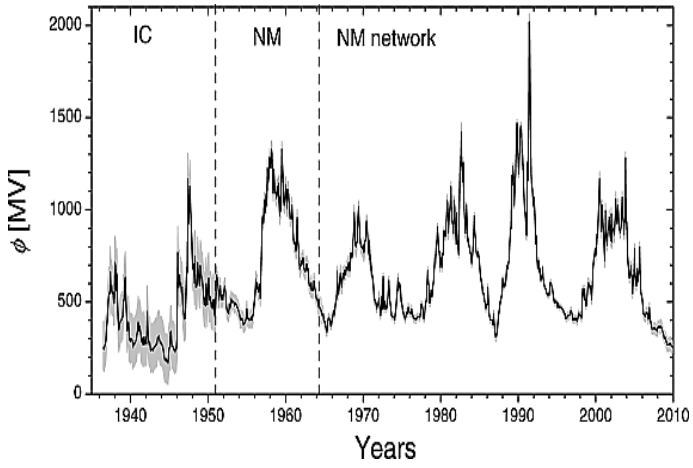

Figure 2.1: Time profile of the reconstructed modulation parameter ϕ together with 68% confidence interval. The vertical dashed lines separate epochs of different instruments used for the reconstruction. [4].

When planning a high energy space mission, the solar phase must be taken into account. In general, a solar maximum is preferred due to the presence of a much stronger solar wind which, by sweeping the Solar System far and wide, ensures lower levels of GCRs, hence a lower background. On the other hand, a stronger solar activity means more intense fluxes of high energy solar particles, which must be taken into account for missions outside the Van Allen Belts; below them, just 1%

of those particles manage to slip through, so that spacecrafts in LEO are not affected by SEP (Fioretti, 2011);

- geomagnetic modulation: a strong, complex attenuation by the Earth's magnetic field which deflects charged particles according to their rigidity. The Earth's magnetic field is produced by currents flowing inside the planet, presumably due to the nucleus, and by magnetic rocks forming the surface. This field can be represented, as a first approximation, by a dipole with an axis tilted of $\sim 11^\circ$ respect to the Earth's rotational axis and shifted of $\sim$450 km respect to its center. [1] Charged particles traversing the Earth's magnetic field undergo a vector force that results in a curved path perpendicular to the momentum of the geomagnetic field, $B_\perp$, with a curvature radius ρ around $B_\perp$ defined as

$$\rho = \frac{R}{B_\perp} = \frac{pc}{B_\perp Ze} \tag{2.1}$$

where pc and Ze are the relativistic momentum and the total charge of the particle respectively and R is the rigidity, defined as momentum per unit charge as follows

$$R = \frac{pc}{Ze} \tag{2.2}$$

[1] The shift between the planet's magnetic and rotational axis is the cause of the so called South Atlantic Anomaly (SAA), an area located in the midst of South Atlantic Ocean extending from South America to the west coast of southern Africa, in which inner Van Allen Radiation Belt comes closest to the Earth's surface leading to an increased flux of energetic particles which exposes orbiting satellites to higher-than-usual levels of radiation. According to most recent measurements, the SAA is both expanding westward and continuing to weaken in intensity, as well as splitting into two lobes (source: https://www.nasa.gov/feature/nasa-researchers-track-slowly-splitting-dent-in-earth-s-magnetic-field), a phenomenon that may be connected with the weakening of the Earth's magnetic field and may also represent a signal of a near future inversion of the magnetic poles. In order to avoid damages during the passage through the SAA, all the sensible satellite's instruments are usually turned off.

Rigidity and kinetic energy are related to each other by the simple relation

$$R = \frac{A}{Ze}\sqrt{E_k^2 + 2mc^2E_k} \tag{2.3}$$

where A is the particle's mass in amu and mc^2 is the rest mass.
The unit of measurement is volt or, often, gigavolt.
Equations 2.1 and 2.3 show the strong correlation between R and E_k and between rigidity and particles' deflection: the higher the rigidity – that is, the kinetic energy – the lower the deflection and, on the contrary, the lower the rigidity the higher the deflection. Hence, from a qualitative view, rigidity provides us useful information about the trend of a particle of being deflected – or even reflected! – by a magnetic field.

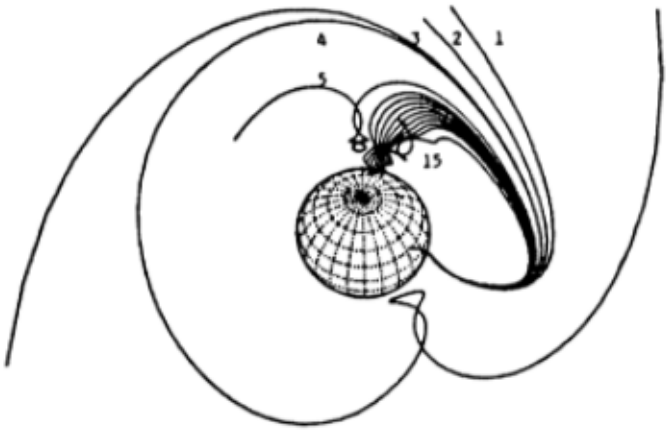

Figure 2.2: Cosmic rays' trajectories depending on rigidities: high rigidity cosmic rays (1) travel relatively simple orbits; as the rigidity of the particle decreases, trajectories become more complicated, forming intermediate loops (4 and 5) and becoming forbidden when intersecting the planet's surface. Note that very low rigidity particles may nevertheless form allowed trajectories (15): the coexistence of allowed and forbidden trajectories forms the cosmic ray penumbra. [5].

Considering protons with kinetic energy of 1 GeV, the equation (2.3) becomes:

$$R = \sqrt{E_k^2[GeV] + 2 \cdot 0.938E_k[GeV]} \simeq 1.7\,GV \tag{2.4}$$

Because this thesis focuses on protons, from now on the GCR flux will be treated as a proton flux.

2.2 The geomagnetic cutoff

Given the relation between deflection and particle kinetic energy, the spectrum of GCRs in LEO exhibits a power law trend at high energies followed by a sharp, strong drop around 1 GeV: we call this the low energy cutoff.

Geomagnetic cutoff rigidities are useful to describe the geomagnetic field's shielding effect and can be calculated for any position by combining the International Geomagnetic Reference Field (IGRF) models to massive computer simulations. The International Geomagnetic Reference Field (IGRF) is a series of mathematical models of the Earth's main field and its annual rate of change, obtained through a large-scale collaboration between modellers and institutes involved in collecting and disseminating magnetic field data from satellites and from observatories and surveys around the world. A particularly important parameter is the g_1^0 coefficient which depends on the Earth's magnetic activity and gives valuable information regarding its magnitude. Such variable is updated every 5 years and its most recent value, finalized by a task force of IAGA (International Association of Geomagnetism and Aeronomy) for the year 2015 is equal to 29442.0 nT; unless indicated otherwise, this value will be used.

Nevertheless, since millions of special case solutions are required to obtain a world-wide set of geomagnetic cutoff rigidities – a formidable effort far beyond our reach – the equation describing the charged particles' motion in the Earth's magnetic field still has no solution in a closed form.

However, it is possible to study the orbital parameters' effect on the geomagnetic cutoff by using the Störmer equation in the approximation of the dipole field geometry:

$$R_c = \frac{M \cos(\lambda)^4}{r^2[1 + \sqrt{(1 - \sin(\epsilon)\sin(\xi)\cos(\lambda)^3}]^2} \tag{2.5}$$

where R_c is the geomagnetic cutoff in GV, M is the magnitude of the dipole moment in G cm^3, λ is the latitude from the magnetic equator, ϵ is the angle from the zenith direction – where the zenith is assumed radial from the position of the dipole center –, ξ is the azimuthal angle measured clockwise from the direction to the north magnetic pole and r is the distance from the dipole center in centimeters. Since the maximum values of flux are detected along the vertical, for many applications only the vertical cutoff is considered, hence $\epsilon = 0$ and this leads to

$$R_c = \frac{M \cos(\lambda)^4}{r^2[1 + \sqrt{(1 - \sin(0)\sin(\xi)\cos(\lambda)^3}]^2} \tag{2.6}$$

where the value of the dipole moment M is defined as

$$M = g_1^0 \cdot R_\oplus^3 \tag{2.7}$$

with g_1^0 in nT taken from the International Geomagnetic Reference Field and $R_\oplus$ representing the average radius of the Earth in cm.
Thus, Equation 2.6 becomes

$$R_c = \frac{g_1^0 \cdot R_\oplus^3}{4} \cdot \frac{cos(\lambda)^4}{r^2} \tag{2.8}$$

and by using normalized units expressing r in Earth radii we obtain

$$R_c = \frac{g_1^0 \cdot R_\oplus}{4} \cdot \frac{cos(\lambda)^4}{r^2/R_\oplus^2} \qquad [GV] \tag{2.9}$$

This equation is expressed in the old mixed CGS units, hence conversion constants 10^9 eV per GV, 10^4 Gauss per Tesla and 1 Statvolt/cm = 300 V/cm per Gauss must be included; for instance, by assuming a g_1^0 value of 29442.0 nT and a $R_\oplus$ of 6371 km, we obtain

$$R_c = \frac{29442 \cdot 10^{-9} \cdot 6371 \cdot 10^5}{4} \cdot \frac{cos(\lambda)^4}{r^2/R_\oplus^2} \qquad [T \cdot cm] \tag{2.10}$$

$$= \frac{29442 \cdot 10^{-5} \cdot 6371 \cdot 10^5}{4} \cdot \frac{cos(\lambda)^4}{r^2/R_\oplus^2} \qquad [G \cdot cm] \tag{2.11}$$

$$= \frac{29442 \cdot 10^{-5} \cdot 300 \cdot 6371 \cdot 10^5}{4} \cdot \frac{cos(\lambda)^4}{r^2/R_\oplus^2} \qquad [V] \tag{2.12}$$

$$= \sim 14.1 \cdot \frac{cos(\lambda)^4}{r^2/R_\oplus^2} \qquad [GV] \tag{2.13}$$

A not intuitive feature regarding the geomagnetic cutoff is that it is not sharp but, on the contrary, "stairways" shaped, as showed in the illustration below, where the cosmic ray penumbra defined in Figure 2.2 is represented:

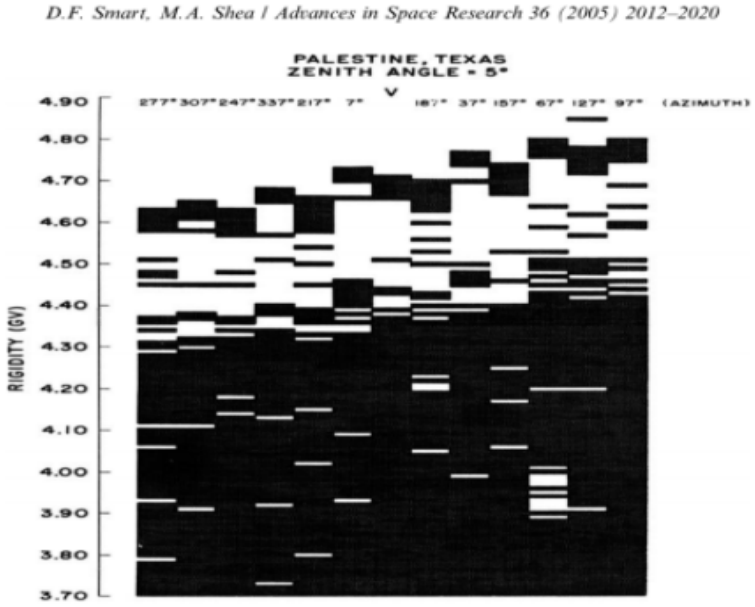

Figure 2.3: The stairways shape of the geomagnetic cutoff given by the penumbra region. White and black spots indicate allowed and forbidden trajectories respectively; as can be seen the CR transmission changes from fully allowed (top) to fully forbidden (bottom), passing through a discrete range in which both allowed and forbidden trajectories are present, the penumbra region [5].

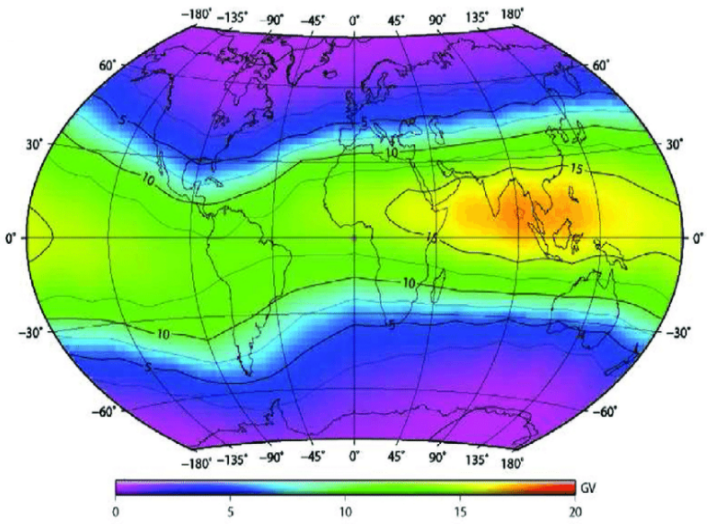

Figure 2.4: Effective geomagnetic cutoff rigidity calculated for the epoch 2010 using the IGRF model [6].

2.3 The LEO protons' model

Mizuno et al. 2004 provides an empirical model built from the AMS-01's data (see chapter 3.1, Alcaraz et al. 2001) which is able to reproduce the primary protons' spectrum for both LEO and balloon flight experiments. Primarily developed for the Gamma-Ray Large Area Space Telescope (GLAST) balloon experiment, it can be also adopted for alpha nuclei, electrons and protons and covers an energy range from ∼10 MeV up to ∼100 GeV.
The core of the model is an analytical function which parameterizes both the solar and geomagnetic modulation as follows:

$$Primary(E_k) = Unmod(E_k{+}Ze\phi) \times \frac{(E_K + Mc^2)^2 - (Mc^2)^2}{(E_k + Mc^2 + Ze\phi)^2 - (Mc^2)^2} \times \frac{1}{1 + (R/R_c)^{-b}} \tag{2.14}$$

where:

- Unmod(E_k+Zeϕ) $= A\left[\frac{R(E_k)}{GV}\right]^{-a}$ describes the protons' spectrum in the interstellar space. Here A = 23.9 counts s^{-1} m^{-2} sr^{-1} MeV^{-1}, E_k is the kinetic energy in GeV, R is the rigidity as function of the kinetic energy in GV and a is an adimensional constant equal to 2.83;
- $\frac{(E_K + Mc^2)^2 - (Mc^2)^2}{(E_k + Mc^2 + Ze\phi)^2 - (Mc^2)^2}$ adds the modulation by the solar wind, hence it depends on the Sun's activity. Here Z is the atomic number of the particle, M is its mass in GeV/c2, e is the electron charge, c is the speed of light and ϕ is the solar modulation parameter in GV;
- $\frac{1}{1 + (R/R_c)^{-b}}$ represents the cutoff due to the Earth's magnetism. Here b is an adimensional constant equal to 12.0 for protons and alpha nuclei and to 6.0 for electrons and positrons, and R_c is the rigidity cutoff in GV calculated assuming the dipole approximation and expressing the distance r from the dipole center in Equation 2.8 as

$$r = h + R_{\oplus} \tag{2.15}$$

where $R_\oplus$ is the Earth's average radius and h is the vehicle's altitude. By normalizing in Earth's radii we finally obtain:

$$R_c = 14.9 \cdot \frac{\cos(\theta_m)^4}{\left(\frac{R_\oplus + h}{R_\oplus}\right)^2} = \tag{2.16}$$

$$= 14.9 \cdot \frac{\cos(\theta_m)^4}{\left(1 + \frac{h}{R_\oplus}\right)^2} \tag{2.17}$$

The model can be used for the entire solar cycle and for the entire low Earth orbit by properly adjusting the ϕ and R_c parameters respectively.

Our goal is now to check the accuracy of the model's previsions by comparing them with the actual measurements obtained by AMS-01 and by the balloon-borne experiments BESS, IMAX and CAPRICE, in order to evaluate the systematical uncertainty introduced when modeling the LEO primary protons' environment. This could let us gain valuable information which can be properly used in the near future to develop better estimates and, eventually, improve the model itself.

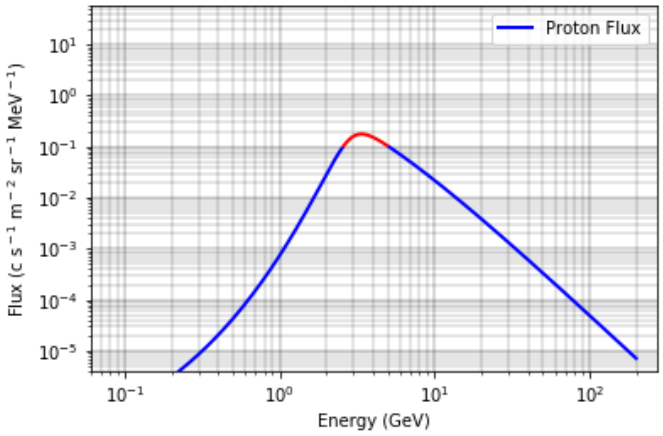

Figure 2.5: Primary protons' flux as modelled by Mizuno et al. 2004 by setting a θ_m of ∼43°, an altitude h of 380 kilometers and a solar modulation parameter ϕ of 550 MV; these values are arbitrary and consistent with a medium latitude LEO mission being operative during a solar minimum.
In the high energy region, the spectrum is well described by a power law, while around 1 GeV a sharp drop is visible; the cutoff region is highlighted in red.

Chapter 3

Comparison with in-flight measurements

The experiments that will be considered are the spaceborne AMS-01 and the balloon-borne BESS, IMAX and CAPRICE; for each, the accuracy of the model with regard to the acquired experimental data will be tested.
The first step consisted in writing a Python code [1]which includes the analytical function described in Section 2.5 and the specific parameters required to obtain the flux, that are:

- an altitude value h, equal to 380 km for AMS-01, to 37 km for BESS, to 36 km for IMAX and varying from 36.1 to 38 kms for CAPRICE;
- a parameter θ_m representing the geomagnetic latitude where measurements are taken; this is equal to 1.14 rad ($\sim$63.5°)[2] for BESS, IMAX and CAPRICE, and varies within a 0 to 1.1 rad (0 to $\sim$63°) range for AMS-01;
- the solar modulation parameter ϕ, equal to 0.55 GV for AMS-01, 0.6 GV for CAPRICE, 0.65 GV for BESS and varying in a 0.7 - 0.8 GV

[1]The Python's code used is open to everyone and can be downloaded at the following link: https://github.com/matteofonsetti/ProtonsCode.git.

[2]Corresponding to Manitoba Lake, Canada.

range for IMAX.

The remaining quantities are constants for all the experiments, and can be summarised as below:

Quantity	Description	Value
R_{Earth}	Earth's radius	6371 km
m	Proton's mass	0.93827208816 GeV/c^2
T_{0p^+}	Proton's rest energy	0.93827208816 GeV

Table 3.1: The constant inputs of the model.

3.1 AMS-01

AMS-01 operated during the STS-91 mission which was flown by Space Shuttle Discovery and launched from Kennedy Space Center, site 39-A, on 2 June 1998. The mission lasted 9 days, 19 hours, 54 minutes and 2 seconds with an orbital period of 91.8 minutes and 51.7° of inclination.
Having collected data in a wide range of energies and geomagnetic latitudes, AMS-01 represents the perfect testing ground for our check, as it allows a thorough investigation across a wide range of orbital positions.
The results obtained are the following:

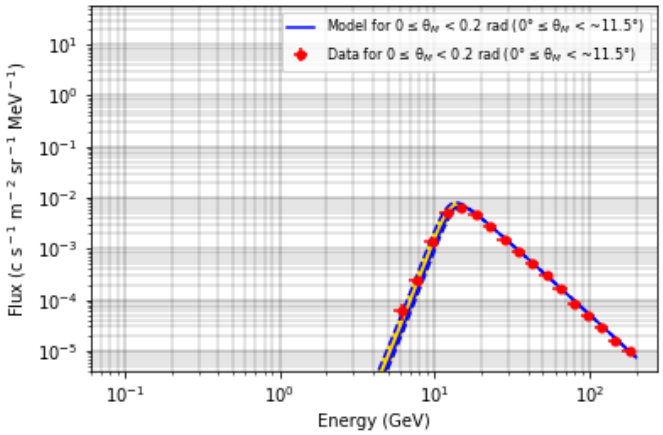

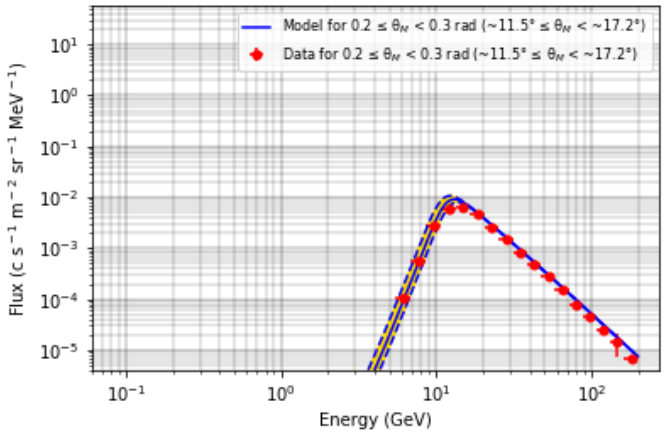
Model for 0.2 ≤ θ_M < 0.3 rad (~11.5° ≤ θ_M < ~17.2°)
Data for 0.2 ≤ θ_M < 0.3 rad (~11.5° ≤ θ_M < ~17.2°)
Flux (c s⁻¹ m⁻² sr⁻¹ MeV⁻¹)
Energy (GeV)

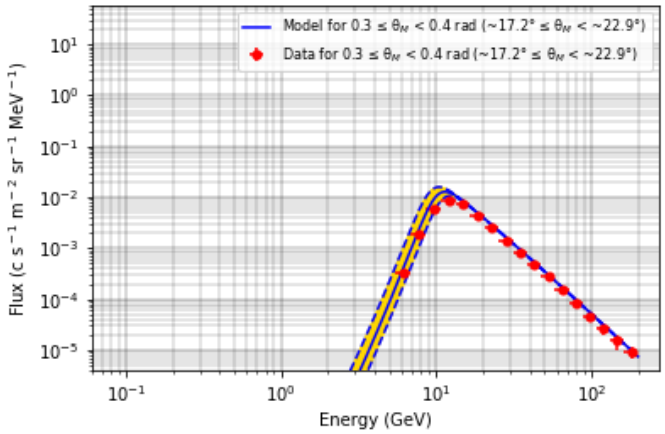
Model for 0.3 ≤ θ_M < 0.4 rad (~17.2° ≤ θ_M < ~22.9°)
Data for 0.3 ≤ θ_M < 0.4 rad (~17.2° ≤ θ_M < ~22.9°)
Flux (c s⁻¹ m⁻² sr⁻¹ MeV⁻¹)
Energy (GeV)

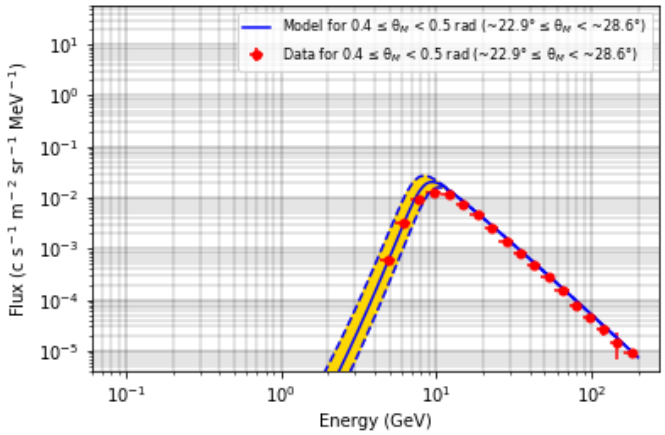
Model for 0.4 ≤ θ_M < 0.5 rad (~22.9° ≤ θ_M < ~28.6°)
Data for 0.4 ≤ θ_M < 0.5 rad (~22.9° ≤ θ_M < ~28.6°)
Flux (c s⁻¹ m⁻² sr⁻¹ MeV⁻¹)
Energy (GeV)

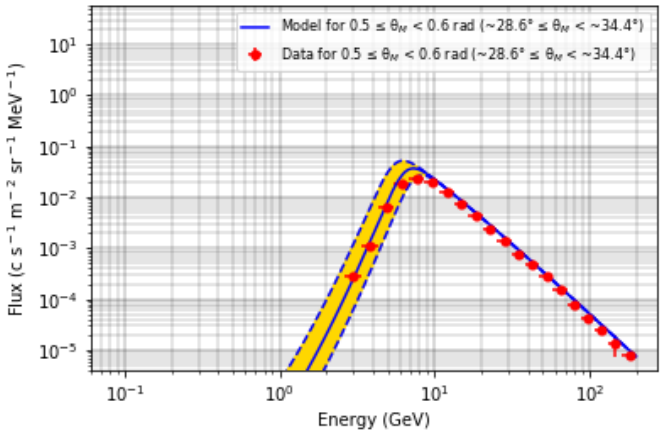
Model for 0.5 ≤ θ_N < 0.6 rad (~28.6° ≤ θ_N < ~34.4°)
Data for 0.5 ≤ θ_N < 0.6 rad (~28.6° ≤ θ_N < ~34.4°)
Flux (c s⁻¹ m⁻² sr⁻¹ MeV⁻¹)
Energy (GeV)

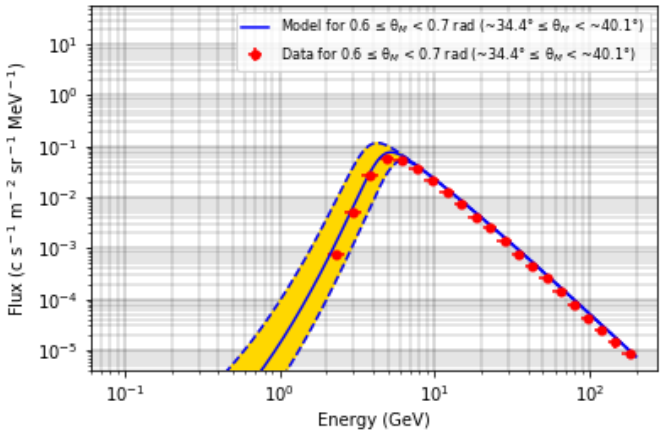
Model for 0.6 ≤ θ_N < 0.7 rad (~34.4° ≤ θ_N < ~40.1°)
Data for 0.6 ≤ θ_N < 0.7 rad (~34.4° ≤ θ_N < ~40.1°)
Flux (c s⁻¹ m⁻² sr⁻¹ MeV⁻¹)
Energy (GeV)

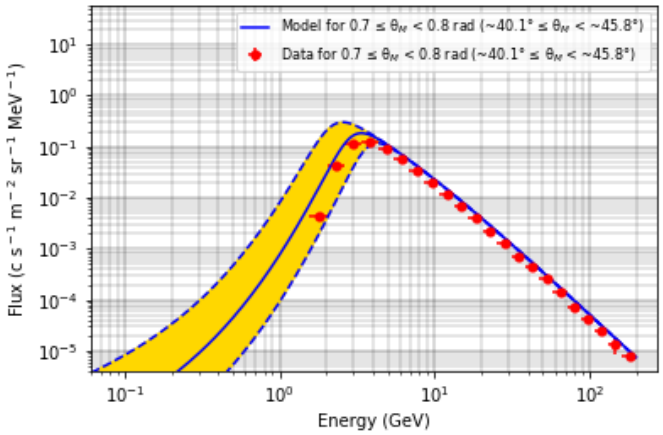
Model for 0.7 ≤ θ_N < 0.8 rad (~40.1° ≤ θ_N < ~45.8°)
Data for 0.7 ≤ θ_N < 0.8 rad (~40.1° ≤ θ_N < ~45.8°)
Flux (c s⁻¹ m⁻² sr⁻¹ MeV⁻¹)
Energy (GeV)

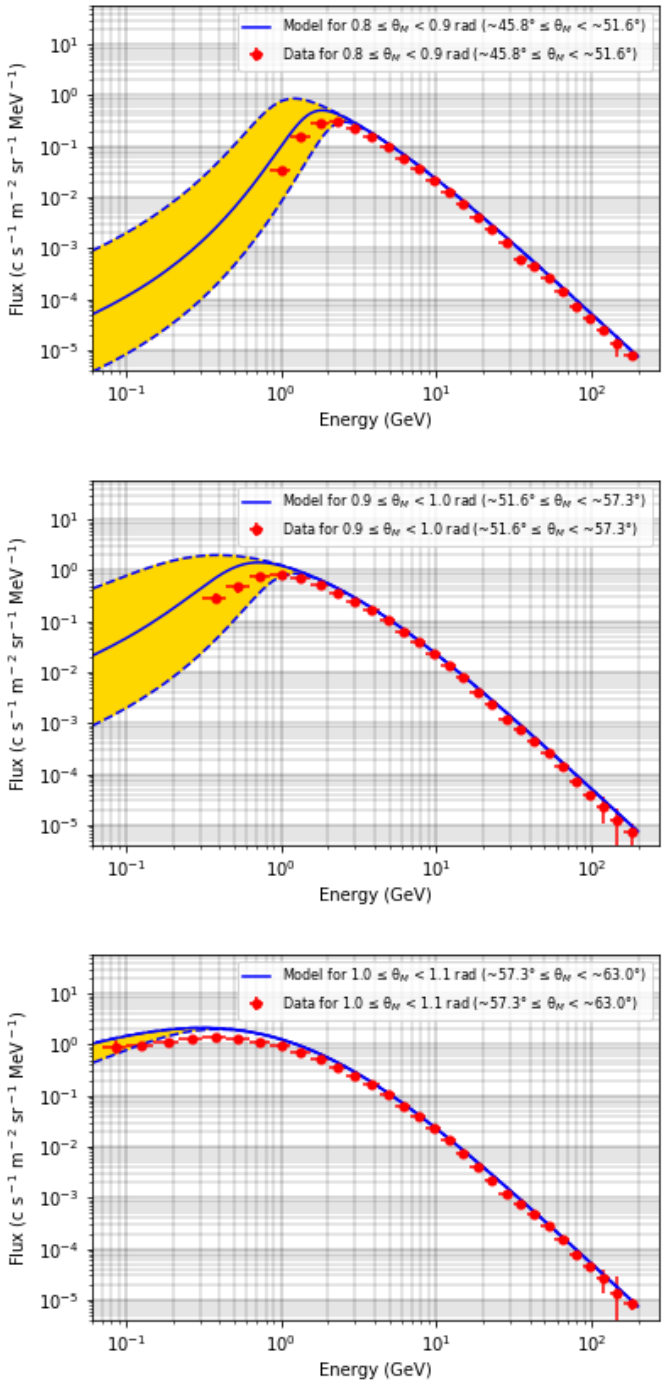

Figure 3.1: Flux spectra according to the geomagnetic latitude θ_m at which they were detected.

Each measurement, related to a certain energy bin, carries an uncertainty in the geomagnetic latitude with data referring to intervals in magnetic latitude

in the 0.1 - 0.2 rad range. In order to take care of these uncertainties, when comparing the measurements with the model, I calculated the flux including the ends of each latitude's interval. For each plot, therefore, the red dots are the experimental data, the blue solid line indicates the model's prevision for a geomagnetic latitude θ_m equal to the average value inside the bin, the dashed lines show the same prevision for a θ_m equal to the minimum and maximum value of the bin, respectively, and the golden area represents all the possible previsions inside the latter twos. The uncertainties on the experimental data are also shown.
We can observe that:

- Data and previsions match more in the high energy region – that is, the power law one – while in the lower energy region – that is, where the geomagnetic cut-off takes place – the gap between model estimates and experimental data increases;

- In the light of the foregoing, experimental data within the lower energy region seem to be more in agreement with the lower dashed flux than with the upper dashed one. This, combined with the results obtained for the IMAX and CAPRICE comparisons which will be shown shortly, may indicate an overestimating trend of the model with respect to the actual data;

- Solid line and dashed lines progressively separate as we approach mid-latitudes, reaching a maximum gap for θ_m $\sim$0.9 rad ($\sim$51°), and then draw closer abruptly, almost coinciding again for high latitudes.
  This means that, given a variation δ in the geomagnetic latitude θ_m and considering the model's estimated flux, the same δ leads to larger discrepancies as the geomagnetic latitude increases; at higher latitudes, around $\sim$63°, the trigonometric $\cos(\theta_m)^4$ term in equation 2.5 becomes very close to zero – assuming zero value precisely for $\theta_m = \pm 90°$, corresponding to the poles – indicating that the cutoff is now practically absent and the flux is no more influenced by the latitude.

On this, I thought it appropriate to carry out a more in-depth investigation. First thing, I considered just three θ_m values, one for low, one for mid and one for high latitudes; these are 14.3°, 37.2° and 65.3°, respectively.
I then chose a value equal to 3% to represent the maximum variation on θ_m so that, given a starting value, this may vary in a ± 3% range.
Finally I run the model and, for each of the three values, flux predictions have been included, obtaining the following result:

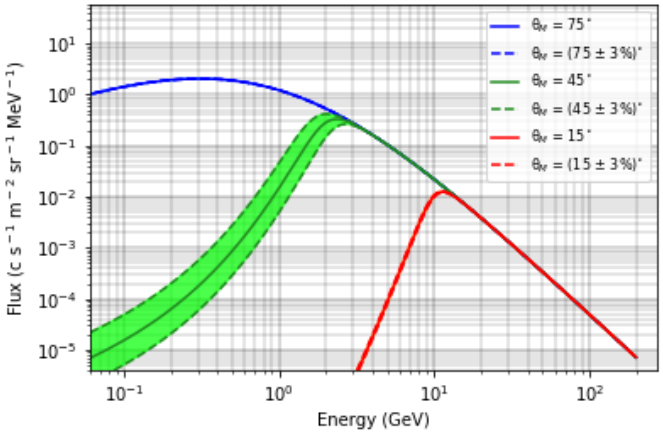

Figure 3.2: Proton spectra for low (red), middle (green) and high (blue) geomagnetic latitudes

The plot clearly shows that while for low latitudes a 3% variation of θ_m leads to almost no difference in the expected flux, the same variation brings to well defined different fluxes at mid latitudes.
Furthermore, as expected at high level latitudes the cutoff effect disappears, hence the blue line in the graph represents a sort of limit beyond which the phenomenon becomes negligible, ceasing to exist for $\theta_m = \pm 90°$.
In order to identify the region in which this phenomenon is more intense, I conducted a more thorough investigation by considering the same variation value and plotting the fluxes for a wide range of θ_m covering the entire mid latitude region [3].

[3] Regarding the term "mid latitude region", I referred to the Middle Latitude's definition itself according to which middle latitudes are located between 23°26′22″ and 66°33′39″ north and 23°26′22″ and 66°33′39″ south. Given that, I've chosen evenly spaced θ_m values varying inside the range above.

The results are the following:

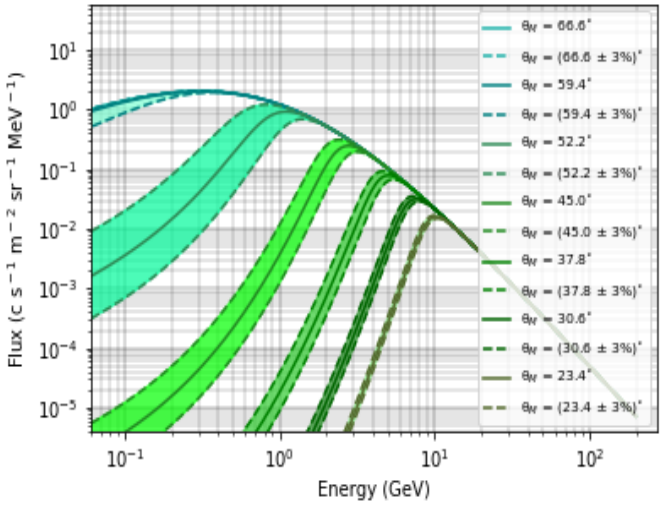

Figure 3.3: Proton spectra depending on different θ_m values inside the middle latitude region.

As can be seen, the same variation δ inside the i-th θ_m produces increasingly pronounced discrepancies in the flux estimated by the model, with a maximum of such discrepancies for a θ_m value above 52.2° and below 57.6°.
Following the plots of Figure 3.1, a thorough calculation of the discrepancies between the model's estimated fluxes and the experimental data was performed.

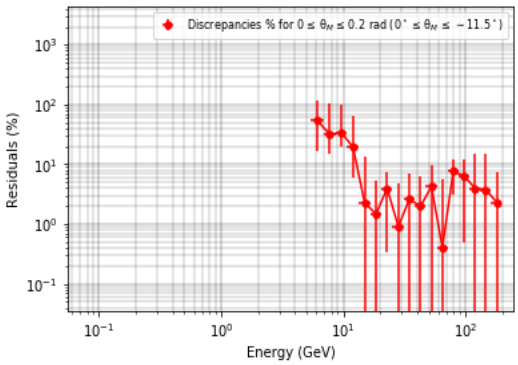

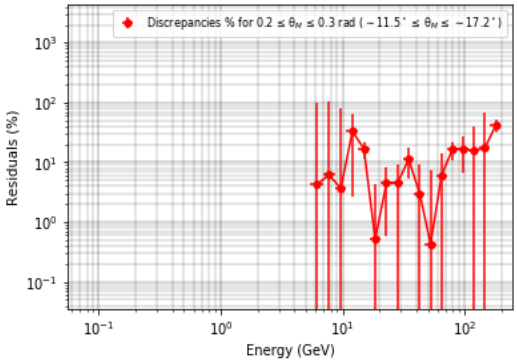
Discrepancies % for 0.2 ≤ θ_N ≤ 0.3 rad (~ 11.5° ≤ θ_N ≤ ~ 17.2°)
Residuals (%)
Energy (GeV)

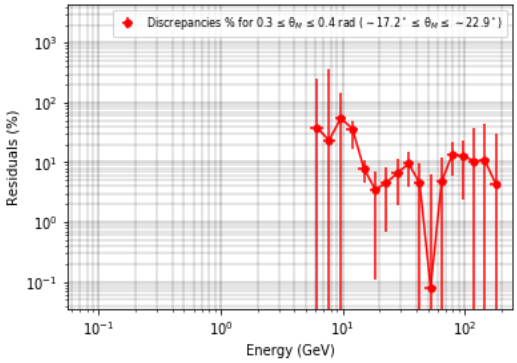
Discrepancies % for 0.3 ≤ θ_N ≤ 0.4 rad (~ 17.2° ≤ θ_N ≤ ~ 22.9°)
Residuals (%)
Energy (GeV)

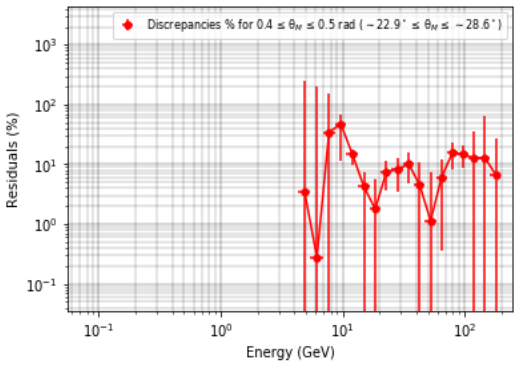
Discrepancies % for 0.4 ≤ θ_N ≤ 0.5 rad (~ 22.9° ≤ θ_N ≤ ~ 28.6°)
Residuals (%)
Energy (GeV)

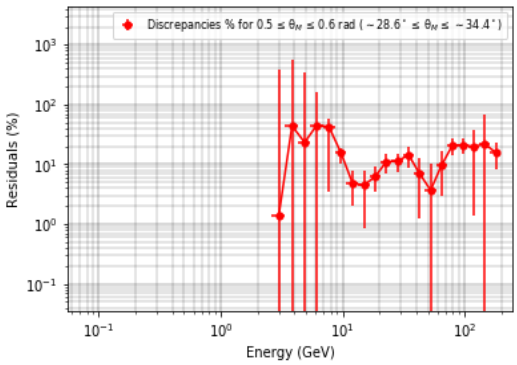
Discrepancies % for 0.5 ≤ θ_N ≤ 0.6 rad (~ 28.6° ≤ θ_N ≤ ~ 34.4°)
Residuals (%)
Energy (GeV)

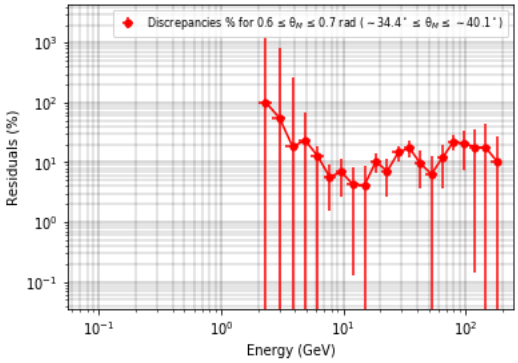
Discrepancies % for 0.6 ≤ θ_M ≤ 0.7 rad (~ 34.4° ≤ θ_M ≤ ~ 40.1°)
Residuals (%)
Energy (GeV)

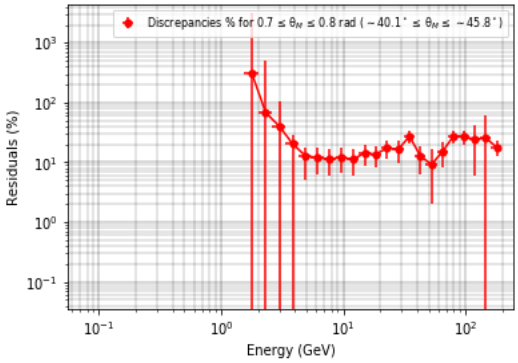
Discrepancies % for 0.7 ≤ θ_M ≤ 0.8 rad (~ 40.1° ≤ θ_M ≤ ~ 45.8°)
Residuals (%)
Energy (GeV)

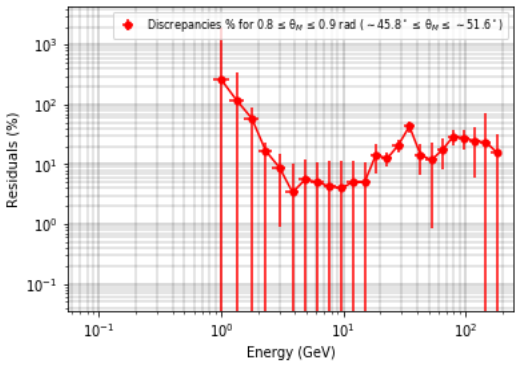
Discrepancies % for 0.8 ≤ θ_M ≤ 0.9 rad (~ 45.8° ≤ θ_M ≤ ~ 51.6°)
Residuals (%)
Energy (GeV)

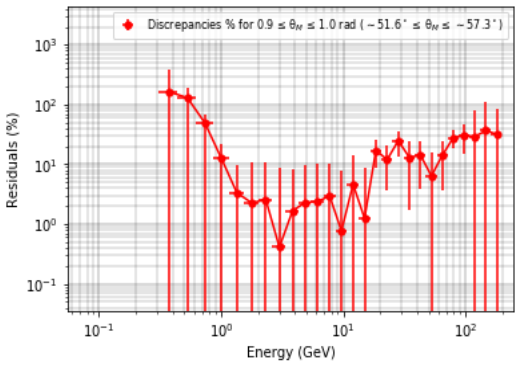
Discrepancies % for 0.9 ≤ θ_M ≤ 1.0 rad (~ 51.6° ≤ θ_M ≤ ~ 57.3°)
Residuals (%)
Energy (GeV)

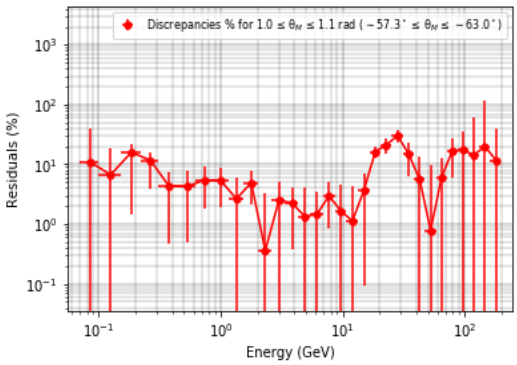

Figure 3.5: Residuals between AMS-01 data and model.

Here the red points represent the percentile ratio of the difference in absolute value between data and estimated average value, compared with the data, while the error bars are obtained by propagating the errors in the measurement and the uncertainty in the magnetic latitude interval. Given a quantity Q given by the difference between a and b with uncorrelated and random errors δa and δb, we have that the error associated to Q adds in quadrature as follows

$$\delta Q = \sqrt{(\delta a)^2 + (\delta b)^2} \tag{3.1}$$

In our case a represents the data uncertainty, while

$$b = |\Phi_i - \phi_i| \tag{3.2}$$

with Φ_i representing the average value of the flux estimated by the model – that is, the one obtained by using the middle value of θ_m – and ϕ_i maximum or minimum value of such flux respectively, that is the ones obtained for the greatest/smallest value of θ_m for the considered energy bin.
The results with three significant digits are shown in Appendix A, with data and model values expressed in $(\mathrm{m}^2\ \mathrm{s\ sr\ MeV})^{-1}$.
We observe that in the power law region the uncertainties set around $\sim$10% while in the cutoff region they tend to increase, overcoming the 100%'s threshold; it must be noted, however, that such higher uncertainties are associated to lower fluxes, hence they have a much lower impact in the total amount of protons reaching the satellite.

3.2 The Balloon Borne Experiments: BESS, IMAX and CAPRICE

The results of my study regarding the balloon-borne experiments BESS-98, IMAX and CAPRICE, which all flew over Lynn Lake, Manitoba, Canada, can be found in Appendix B.

It's worth noting that now, despite being the same environment we find in LEO, a small attenuation in the measured flux due to the interaction of primaries with air is present and must be taken into account; for this dissertation, I opted for a 4% air attenuation as suggested for the BESS-98 experiment (Mizuno et al. 2004), as the other balloon-borne experiments flew at similar altitudes and at the same latitude [4].

BESS (Balloon-borne Experiment with a Superconducting Spectrometer) flew in 1998 (ϕ = 650 MV) at an altitude of 37 km collecting highly precise measurements in a 1-120 GeV energy range (Sanuki et al. 2000).

Since the range covered by BESS-98 does not reach the cutoff region, this experiment gives us information only regarding the power law region for which the model provides estimates in good agreement with data, steadily remaining below a ∼10% discrepancy's percentage:

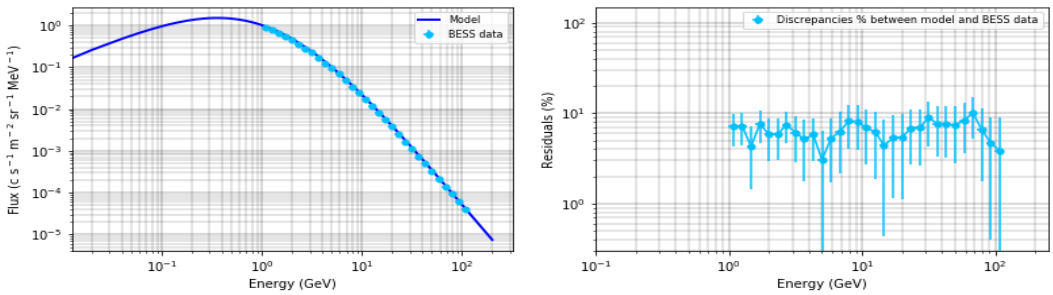

Figure 3.6: Protons' spectra for BESS (light blue) and model (blue) (left) and residuals (right).

IMAX (Isotope Matter-Antimatter Experiment) flew in 1992 at an altitude

[4] ∼65.8°, corresponding to Manitoba Lake, Canada.

of 36 km measuring a protons' spectrum ranging from 0.2 GeV to 200 GeV (Menn et al. 2000). An interesting feature in this experiment is that we don't have an exact value for the solar parameter ϕ but just an approximation within a 0.7 - 0.8 GV range, this gives us the opportunity to check how deeply the solar modulation may affect the results. For this purpose, I decided to consider an average value $\phi = 0.75$ GV, a minimum value $\phi_- = 0.70$ GV and a maximum value $\phi_+ = 0.80$ GV. running the model for each. The fluxes' outcomes are highlighted by the solid enlarged green line, while the dashed blue line represents the result for the average value of ϕ. The rates of the discrepancies steadily remain below 50%.

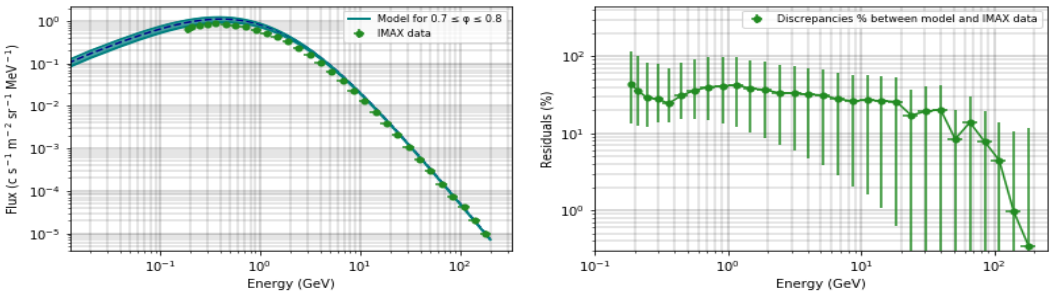

Figure 3.7: Protons' spectra for IMAX (green) and model (blue) (left) and residuals (right). The enlarged green line represents all the model's estimates within the ϕ range considered, blue dashed line corresponds to $\phi = 0.75$ GV.

CAPRICE (Cosmic AntiParticle Ring Imaging Cherenkov) flew on 1994 August 8-9 ($\phi \sim$600 MV), covering an energy range of 0.15 to 200 GeV (Boezio et al. 1999); here, the uncertainty is concerned with altitude, which varies from ∼36.1 to ∼38.0 km, an opportunity to check, this time, how different altitudes may produce different outcomes.

The plot below, which I reproduced using my Python's code taking as example the same plot presented in Cumani et Al. 2019, clearly shows that variations of hundreds of kilometers only lightly affect the obtained flux, which reveals itself to be more susceptible to latitude variations than to altitudes ones.

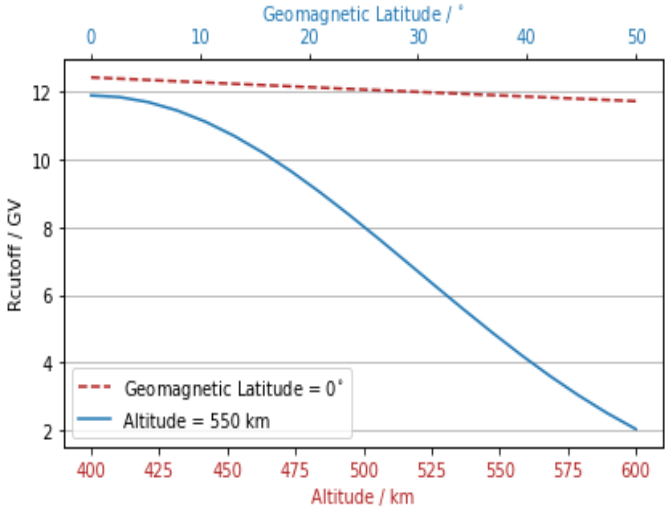

Figure 3.8: Cutoff rigidity values for changing latitude with constant altitude (50 kms, light blue) and for changing altitude with constant latitude (0°, red) [7]

We therefore expect that even by varying the altitude's values inside the given range the resulting flux will remain virtually unchanged, and so it happens, as showed in the plot below where in fact the three fluxes appear almost perfectly overlapped:

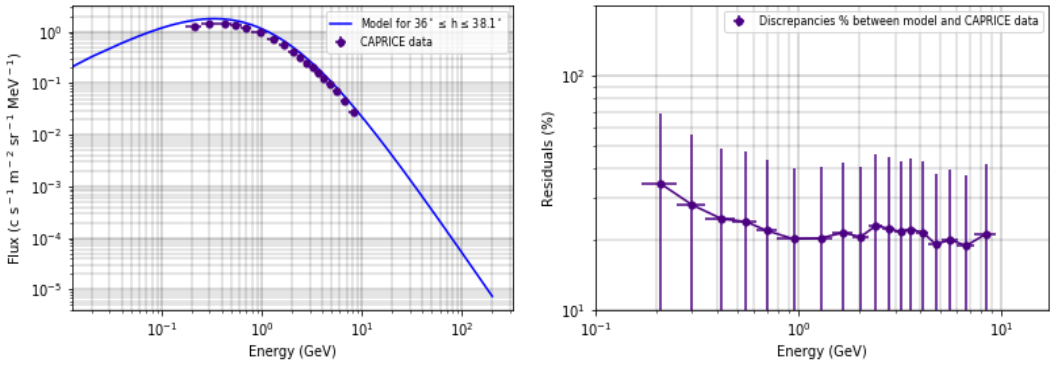

Figure 3.9: Protons' spectra for CAPRICE (indigo) and model (36 - 38.1 altitude range, blue) (left) and residuals (right).

Here uncertainties set around ∼20% in the power law region, slightly increasing in correspondence of the cutoff where they set between ∼20% and ∼30%, reaching ∼35% for the lowest energy bin. At last, both for IMAX and

3.2 The Balloon Borne Experiments: BESS, IMAX and CAPRICE33

CAPRICE reappears the trend seen in the case of AMS-01, as data steadily set below the model's previsions: this may indicates that the model provides an overestimation of the experimental data.
An overview of the relevant missions parameters, including the previous considered AMS-01 for completeness, is shown in Appendix B.

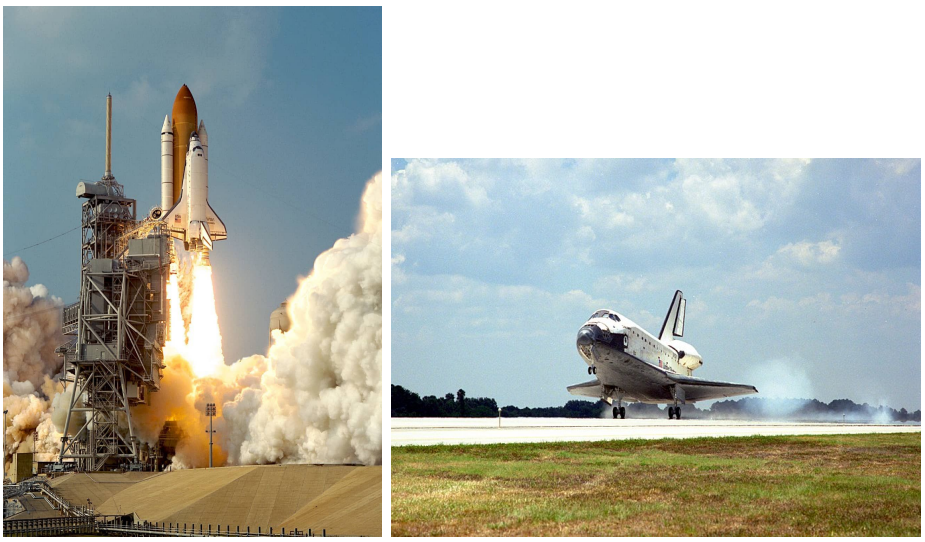

Figure 3.10: STS-91's lift-off and landing at Cape Canaveral, Florida. It was the final Space Shuttle mission to the Mir space station.

Figure 3.11: The Lynn Lake Airport, located at 1070 km NW of Winnipeg, Manitoba, Canada, the launch site for the BESS-98, IMAX and CAPRICE experiments.

Chapter 4

An application to a near future LEO mission

The model presented above will now be used to estimate the primary protons' flux for a satellite mission operating in LEO in the near future. The mission I chose to consider is the X-ray Imaging and Spectroscopy Mission (XRISM), whose launch is expected for January 2022. XRISM will investigate celestial X-ray objects, providing breakthroughs in the study of structure formation of the universe, outflows from galaxy nuclei and dark matter [8]. Its average altitude will be of 550 $\pm$ 50 kilometers with an orbital inclination of 31 degrees [9].

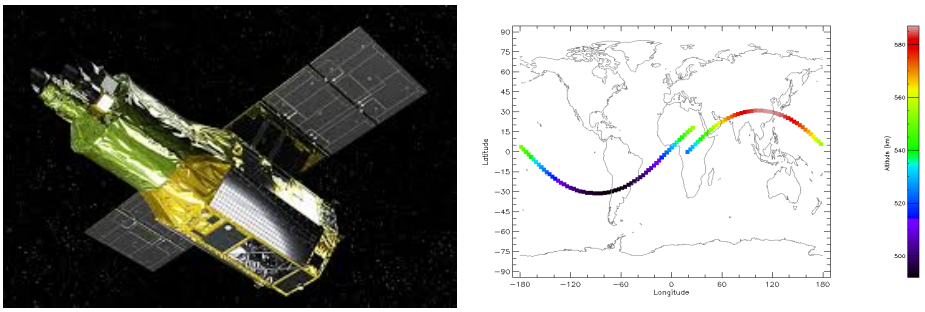

Figure 4.1: a) An artistic view of the XRISM telescope and b) The XRISM's orbit obtained using SPENVIS [1].

[1]https://www.spenvis.oma.be/

I will consider a solar modulation's parameter ϕ equal to 550 MV, which is quite realistic bearing in mind that in 2022 we will be at the beginning of a new solar cycle (the 25-th), and a geomagnetic latitude value θ_m of 0.1 rad, corresponding to $\sim 5.7°$.

As reported in Chapter 2.2, the magnitude of the geomagnetic field using the dipole approximation can be quantified by the g_1^0 parameter which, according to the field itself, varies with time; a proper update of such value needs therefore to be constantly done, and the task is carried out by the International Association of Geomagnetism and Aeronomy, which takes care of determining the new g_1^0's estimates once every 5 years.

The most recent value available dates back to 2015, hence the next one is still missing; this means that, at the time I am writing this dissertation, we still do not have an official g_1^0 value for the year 2022, when XRISM mission will start; nevertheless, a rough estimate to be used here can still be afforded.

As a first step, by plotting the available g_1^0 coefficients [10] we obtain the graphic below, representing a source of valuable information regarding the trend at which the geomagnetic field is changing:

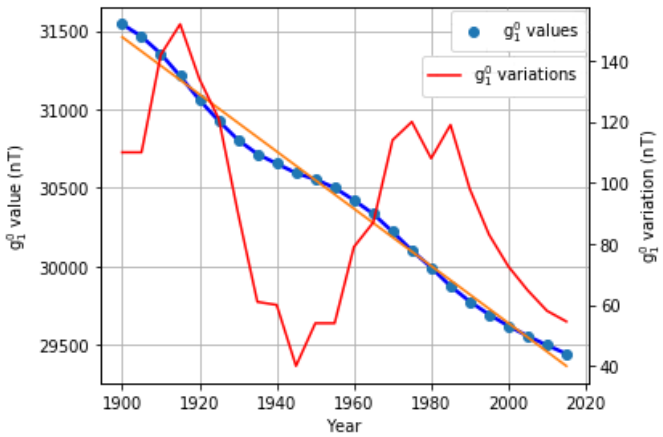

Figure 4.2: The available g_0^1 coefficients spanning from 1900 to 2015 (blue line) and their variations from interval to interval (red line). The orange line represents the line of best fit.

As shown by the solid blue line, the strength of the Earth's magnetic field is constantly decreasing with time; interesting clues about how this trend

develops may be given by the red line, obtained by considering two consecutive values at a time and subtracting the latter to the first; what we gain is the trend at which the g_0^1 values' variation proceeded in the last century, a trend that seems to exhibit some sort of pulsating rate. It must however be noted that the variation of the Earth's magnetic field is an event which takes place on a timescale of thousands of years [11], hence the red line in the plot may just represents a negligible fluctuation inside a much greater and totally different scenario. By now plotting a line of best fit (orange), it becomes possible to extract an approximated g_1^0 value for the near future:

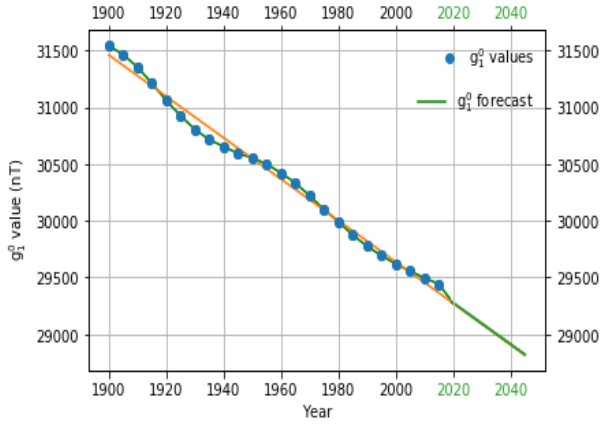

Figure 4.3: G_1^0 coefficients at 5-yrs interval spanning from 1900 to 2015 (blue line) and average forecast from 2020 to 2045 (green line).

The equation of the line of best fit is

$$y = -18.23x + 6.61 \times 10^4 \tag{4.1}$$

from which by substituting into x the corresponding year we can obtain the estimated g_1^0 value needed. The calculated g_1^0's estimates for the 2020-2045 period are reported in Appendix C, including related uncertainties which has been determined by computing the average of the discrepancies between the g_1^0 official values and the line of best fit's corresponding estimates; for 2022, I obtained a g_1^0 of 29238.94 $\pm$ 50 nT and, by substituting it in Equation 2.5, the quantity M returns a value of ~ 14.

The Equation 2.8

$$Primary(E_k) = Unmod(E_k + Ze\phi) \times \frac{(E_K + Mc^2)^2 - (Mc^2)^2}{(E_k + Mc^2 + Ze\phi)^2 - (Mc^2)^2} \times \frac{1}{1 + (R/R_c)^{-b}} \tag{4.2}$$

will now be used using XRISM's related parameters, which are an altitude h of $\sim$ 550 kilometers, a geomagnetic latitude θ_m of 0.1 rad ($\sim 5.7°$), a solar parameter ϕ of 550 MV and a g_1^0 parameter of 29238.94 nT.
Regarding the uncertainties three different approaches are going to be followed:

- the worst scenario possible, a highly conservative approach which consists in considering only the greater uncertainties for each AMS-01's energy bin and apply such uncertainties to the obtained XRISM's flux;

- a more realistic scenario, consisting in propagating for each of the XRISM's energy bins the same uncertainty ratios obtained for the corresponding AMS-01's data;

- an averaged scenario between the upper twos, consisting in considering for each AMS-01's energy bin an average value of the uncertainties obtained both for the upper and the lower estimates respectively.

For all the three scenarios, the experiment whose results are going to be used to build XRISM's predictions is AMS-01, due to the fact that the latter will work in orbit and therefore all the interactions with the atmosphere must not be taken into account.
The results are shown below:

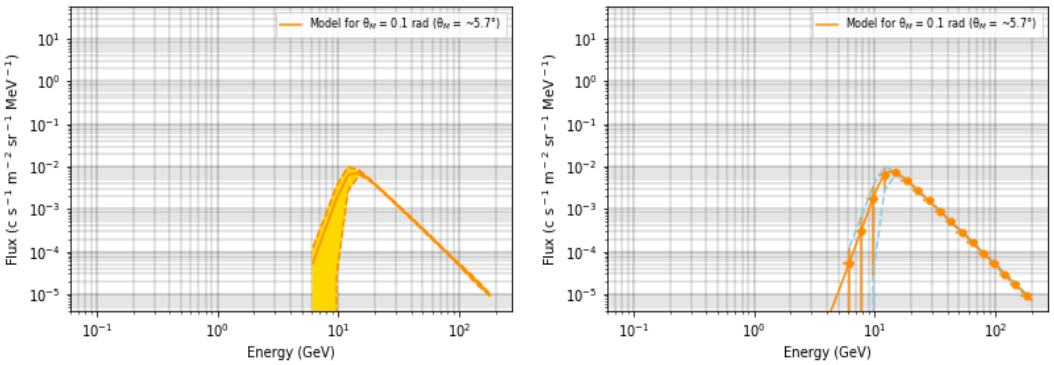

Figure 4.4: Estimated protons' flux for XRISM for $\theta_m = 0.1$ rad ($\sim 5.7°$) and h = 550 km by considering the worst scenario possible, shown both as range (left panel) and as errors to the model.

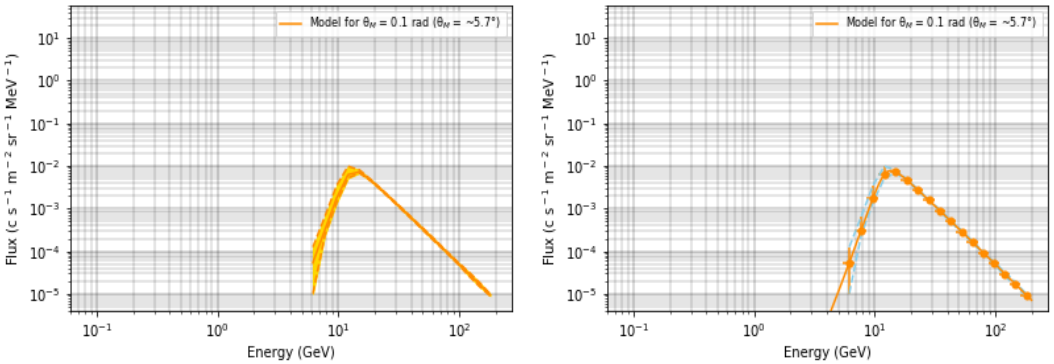

Figure 4.5: Estimated protons' flux for XRISM for $\theta_m = 0.1$ rad ($\sim 5.7°$) and h = 550 km by using the realistic approach, shown both as range (left panel) and as errors to the model.

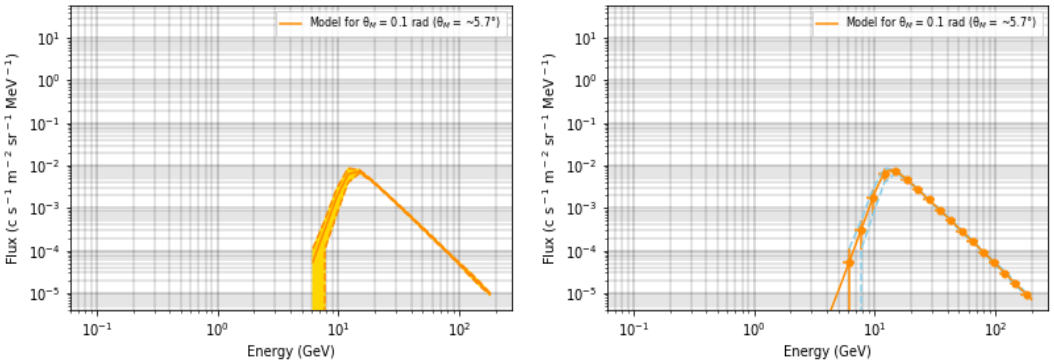

Figure 4.6: Estimated protons' flux for XRISM for $\theta_m = 0.1$ rad ($\sim 5.7°$) and h = 550 km by using the averaged discrepancies, shown both as range (left panel) and as errors to the model.

As we can see, the conservative approach – although returning consistent results – proves to be "too conservative", as it allows a flux near the cutoff

region which may also be equal to zero, a prediction which is unlikely to happen. The use of averaged discrepancies still result in larger errors for the low energy range of the model with respect to the more realistic approach. These behaviours are given by the fact that, as reported in Figure 3.1, the average estimated flux for the considered geomagnetic latitude is much closer to the one obtained for the lower θ_m value compared to the one obtained for the higher, hence by computing the discrepancy for the central latitude value of the interval (the averaged approach) overestimates the lower error.

The realistic approach, which propagates both the upper and lower discrepancy levels given by the two extremes of the latitude's interval, allows to take into account the position of the measured flux by AMS 01 with respect to the model.

The conservative and averaged approaches both grant highly safe estimates at the cost of less accuracy near the cutoff region while the realistic one results in a much higher accuracy.

However, the realistic case requires to evaluate for each chosen latitude the position of the measured flux with respect to the model in order to apply the errors accordingly.

Tables with the results obtained for the considered altitude and geomagnetic latitude and for each of the three approaches are reported in Appendix C.

The extended set of estimates covering the entire satellite's orbit and the entire mission duration can be obtained by simply adjusting ϕ, h and θ_m, respectively.

Chapter 5

Conclusions

The common thread of the entire dissertation has been the evaluation of the primary protons' flux in low Earth orbit, a piece which arranges in a much more vast and complex puzzle represented by the study and the minimization of the background noise in high energy space.
The algorithm which represents the actual state-of-the-art in modeling primary charged particle spectra has been presented in Chapter 2 and compared to actual experiments in Chapters 3 in order to investigate its accuracy with regards to the actual data.
Considering the AMS-01 experiment, the model reproduces the experimental data within an average discrepancy of $\sim$10% inside the power law region overcoming the 100% threshold near the cutoff where, however, the fluxes are lower.
In the case of the balloon-borne experiments BESS-98, IMAX and CAPRICE, the model's outcomes steadily set below 10%, 50% and 35%, respectively, with the highest values again associated to the lowest energy bins.
To complete our analysis, an application of the model to a near future scenario has been presented in Chapter 4 considering the XRISM mission, nominally expected to start in January 2022. Due to the fact that a g_1^0 official value for the year 2022 is not yet available, I extracted a rough value by considering the trend of the ones at our disposal, and used it to calculate the estimated

flux for a specific geomagnetic latitude θ_m equal to 0.1 rad corresponding to $\sim$ 5.7° by adopting for the uncertainties' calculation three different approaches based on the AMS-01's results: a conservative approach which assumes the worst scenario possible, a realistic approach which propagates both the uncertainties obtained for the AMS-01's upward and downward flux onto the new estimated flux obtained for XRISM, and an averaged approach which represents a middle ground between the previous twos.
The obtained results are reported in Figures 4.4, 4.5 and 4.6 and in Appendix C, together with the g_1^0 values calculated for the period from 2020 to 2045.
Extended set of results which include the entire operational orbit and the entire mission duration can be obtained by properly adjusting the entries in Equation 2.5 and 2.8.
The present work is a first step in the evaluation of the systematic uncertainty in current models for the LEO space radiation environment, and future improvements to these results include:

- integrating in energy all the flux and compute the related total errors;
- extending the study to all the other particle populating the LEO environment;
- computing the impact of the model systematic uncertainties in the instrumental background uncertainty.

Appendix A

Comparison with AMS-01 data

$0 \leq \theta m \leq 0.2$ rad ($0 \leq \theta m \leq \sim 11.5°$)

Bin (GeV)	η (%)	Data	Model	δF_i	δF_{i+}	δF_{i-}	$\delta F_{i\%}$	$\delta F_{i+\%}$	$\delta F_{i-\%}$
0.07 - 0.10	-	-	-	-	-	-	-	-	-
0.10 - 0.15	-	-	-	-	-	-	-	-	-
0.15 - 0.22	-	-	-	-	-	-	-	-	-
0.22 - 0.31	-	-	-	-	-	-	-	-	-
0.31 - 0.44	-	-	-	-	-	-	-	-	-
0.44 - 0.62	-	-	-	-	-	-	-	-	-
0.62 - 0.85	-	-	-	-	-	-	-	-	-
0.85 - 1.15	-	-	-	-	-	-	-	-	-
1.15 - 1.54	-	-	-	-	-	-	-	-	-
1.54 - 2.02	-	-	-	-	-	-	-	-	-
2.02 - 2.62	-	-	-	-	-	-	-	-	-
2.62 - 3.38	-	-	-	-	-	-	-	-	-
3.38 - 4.31	-	-	-	-	-	-	-	-	-
4.31 - 5.45	-	-	-	-	-	-	-	-	-
5.45 - 6.86	0.728	$(6.1 \pm 2.2) \times 10^{-5}$	2.81×10^{-5}	3.29×10^{-5}	3.00×10^{-5}	6.01×10^{-5}	53.9	60.9	37.4
6.86 - 8.60	0.899	$(23.7 \pm 2.1) \times 10^{-5}$	16.1×10^{-5}	7.57×10^{-5}	1.71×10^{-4}	3.44×10^{-5}	31.9	72.5	17.0
8.60 - 10.73	1.10	$(138 \pm 6.8) \times 10^{-5}$	91.4×10^{-5}	4.66×10^{-4}	8.97×10^{-4}	18.9×10^{-4}	65.2	13.4	14.6
10.73 - 13.34	1.35	$(49.5 \pm 1.8) \times 10^{-4}$	39.9×10^{-4}	9.60×10^{-4}	8.97×10^{-4}	6.40×10^{-4}	19.4	46.4	13.4
13.34 - 16.55	1.66	$(65.7 \pm 2.1) \times 10^{-4}$	64.2×10^{-4}	1.50×10^{-4}	2.27×10^{-3}	3.11×10^{-4}	2.28	10.9	5.71
16.55 - 20.48	2.03	$(45.7 \pm 1.7) \times 10^{-4}$	45.0×10^{-4}	6.73×10^{-5}	6.86×10^{-4}	2.61×10^{-5}	3.47	3.61	3.61
20.48 - 25.29	2.48	$(27.7 \pm 1.0) \times 10^{-4}$	26.6×10^{-4}	1.09×10^{-4}	2.82×10^{-6}	1.48×10^{-6}	3.95	3.81	3.81
25.29 - 31.20	3.05	$(155 \pm 5.9) \times 10^{-5}$	154×10^{-5}	1.41×10^{-5}	1.51×10^{-7}	7.95×10^{-8}	0.909	4.53	4.53
31.20 - 38.43	3.73	$(90.5 \pm 4.1) \times 10^{-5}$	88.1×10^{-5}	2.37×10^{-5}	7.94×10^{-9}	4.18×10^{-9}	2.62	4.28	4.28
38.43 - 47.30	4.58	$(51.4 \pm 2.2) \times 10^{-5}$	50.4×10^{-5}	1.01×10^{-5}	4.12×10^{-10}	2.18×10^{-10}	1.97	5.67	5.67
47.30 - 58.16	5.61	$(30.0 \pm 1.7) \times 10^{-5}$	28.7×10^{-5}	1.28×10^{-5}	2.12×10^{-11}	1.12×10^{-11}	4.26	5.37	5.37
58.16 - 71.48	6.88	$(164 \pm 8.8) \times 10^{-6}$	163×10^{-6}	6.62×10^{-7}	1.08×10^{-12}	5.69×10^{-13}	0.403	4.53	4.53
71.48 - 87.79	8.42	$(86.1 \pm 3.9) \times 10^{-6}$	92.7×10^{-6}	6.61×10^{-6}	5.47×10^{-14}	2.88×10^{-14}	7.67	4.53	4.53
87.79 - 107.78	10.3	$(49.4 \pm 2.9) \times 10^{-6}$	52.5×10^{-6}	3.14×10^{-6}	2.75×10^{-15}	1.45×10^{-15}	6.35	5.87	5.87
107.78 - 132.27	12.7	$(28.6 \pm 3.1) \times 10^{-6}$	29.7×10^{-6}	1.14×10^{-6}	1.38×10^{-16}	7.27×10^{-17}	3.97	10.8	10.8
132.27 - 162.29	15.5	$(16.2 \pm 1.8) \times 10^{-6}$	16.8×10^{-6}	6.11×10^{-7}	6.90×10^{-18}	3.63×10^{-18}	3.77	11.1	11.1
162.29 - 199.06	19.0	$(97.2 \pm 5.1) \times 10^{-7}$	95.0×10^{-7}	2.24×10^{-7}	3.44×10^{-19}	1.80×10^{-19}	2.31	5.25	5.25

$0.2 \leq \theta\mathrm{m} \leq 0.3$ rad ($\sim 11.5^\circ \leq \theta\mathrm{m} \leq \sim 17.2^\circ$)

Bin (GeV)	η (%)	Data	Model	δF_i	δF_{i+}	δF_{i-}	δF_i%	δF_{i+}%	δF_{i-}%
0.07 - 0.10	-	-	-	-	-	-	-	-	-
0.10 - 0.15	-	-	-	-	-	-	-	-	-
0.15 - 0.22	-	-	-	-	-	-	-	-	-
0.22 - 0.31	-	-	-	-	-	-	-	-	-
0.31 - 0.44	-	-	-	-	-	-	-	-	-
0.44 - 0.62	-	-	-	-	-	-	-	-	-
0.62 - 0.85	-	-	-	-	-	-	-	-	-
0.85 - 1.15	-	-	-	-	-	-	-	-	-
1.15 - 1.54	-	-	-	-	-	-	-	-	-
1.54 - 2.02	-	-	-	-	-	-	-	-	-
2.02 - 2.62	-	-	-	-	-	-	-	-	-
2.62 - 3.38	-	-	-	-	-	-	-	-	-
3.38 - 4.31	-	-	-	-	-	-	-	-	-
4.31 - 5.45	-	-	-	-	-	-	-	-	-
5.45 - 6.86	0.73	$(105 \pm 8.7) \times 10^{-6}$	104×10^{-6}	4.45×10^{-6}	9.71×10^{-5}	4.25×10^{-5}	4.24	92.8	41.3
6.86 - 8.60	0.899	$(53.8 \pm 2.7) \times 10^{-5}$	57.1×10^{-5}	3.34×10^{-5}	5.37×10^{-4}	2.39×10^{-4}	6.20	100	44.8
8.60 - 10.73	1.10	$(28.6 \pm 1.7) \times 10^{-4}$	29.6×10^{-4}	1.04×10^{-4}	2.22×10^{-3}	11.5×10^{-3}	3.65	77.7	40.7
10.73 - 13.34	1.35	$(60.9 \pm 2.4) \times 10^{-4}$	80.9×10^{-4}	2.00×10^{-3}	1.97×10^{-3}	18.3×10^{-3}	32.8	32.6	30.3
13.34 - 16.55	1.66	$(63.4 \pm 1.8) \times 10^{-4}$	74.2×10^{-4}	1.08×10^{-3}	2.27×10^{-4}	3.14×10^{-4}	17.0	4.57	5.71
16.55 - 20.48	2.03	$(45.5 \pm 1.7) \times 10^{-4}$	45.7×10^{-4}	2.33×10^{-5}	1.37×10^{-5}	2.03×10^{-5}	0.513	3.75	3.76
20.48 - 25.29	2.48	$(25.5 \pm 1.0) \times 10^{-4}$	26.6×10^{-4}	1.15×10^{-4}	7.53×10^{-7}	1.12×10^{-6}	4.50	3.92	3.92
25.29 - 31.20	3.05	$(147 \pm 7.1) \times 10^{-5}$	154×10^{-5}	6.61×10^{-5}	4.02×10^{-8}	5.99×10^{-8}	4.50	4.83	4.83
31.20 - 38.43	3.73	$(79.2 \pm 4.7) \times 10^{-5}$	88.1×10^{-5}	8.93×10^{-5}	2.11×10^{-9}	3.15×10^{-9}	11.3	5.93	5.93
38.43 - 47.30	4.58	$(48.9 \pm 3.0) \times 10^{-5}$	50.4×10^{-5}	1.49×10^{-5}	1.10×10^{-10}	1.63×10^{-10}	3.04	6.13	6.13
47.30 - 58.16	5.61	$(28.6 \pm 2.0) \times 10^{-5}$	2.87×10^{-5}	1.23×10^{-6}	6.00×10^{-12}	8.00×10^{-12}	0.429	6.99	6.99
58.16 - 71.48	6.88	$(15.4 \pm 1.2) \times 10^{-5}$	16.3×10^{-5}	9.34×10^{-6}	0	0	6.06	7.79	7.79
71.48 - 87.79	8.42	$(79.6 \pm 4.7) \times 10^{-6}$	92.7×10^{-6}	1.31×10^{-5}	0	0	16.5	5.90	5.90
87.79 - 107.78	10.3	$(45.0 \pm 4.6) \times 10^{-6}$	52.5×10^{-6}	7.54×10^{-6}	0	0	16.8	10.2	10.2
107.78 - 132.27	12.6	$(25.7 \pm 6.1) \times 10^{-6}$	29.7×10^{-6}	4.04×10^{-6}	0	0	15.7	23.7	23.7
132.27 - 162.29	15.5	$(14.3 \pm 7.0) \times 10^{-6}$	16.8×10^{-6}	2.51×10^{-6}	0	0	17.6	49.0	49.0
162.29 - 199.06	19.0	$(84.4 \pm 6.7) \times 10^{-7}$	94.6×10^{-7}	2.80×10^{-6}	0	0	41.7	10.0	10.0

$0.3 \leq \theta\mathrm{m} \leq 0.4$ rad ($\sim 17.2° \; \theta\mathrm{m} \leq \sim 22.9°$)

Bin (GeV)	η (%)	Data	Model	δF_i	δF_{i+}	δF_{i-}	δF_i%	δF_{i+}%	δF_{i-}%
0.07 - 0.10	-	-	-	-	-	-	-	-	-
0.10 - 0.15	-	-	-	-	-	-	-	-	-
0.15 - 0.22	-	-	-	-	-	-	-	-	-
0.22 - 0.31	-	-	-	-	-	-	-	-	-
0.31 - 0.44	-	-	-	-	-	-	-	-	-
0.44 - 0.62	-	-	-	-	-	-	-	-	-
0.62 - 0.85	-	-	-	-	-	-	-	-	-
0.85 - 1.15	-	-	-	-	-	-	-	-	-
1.15 - 1.54	-	-	-	-	-	-	-	-	-
1.54 - 2.02	-	-	-	-	-	-	-	-	-
2.02 - 2.62	-	-	-	-	-	-	-	-	-
2.62 - 3.38	-	-	-	-	-	-	-	-	-
3.38 - 4.31	-	-	-	-	-	-	-	-	-
4.31 - 5.45	-	-	-	-	-	-	-	-	-
5.45 - 6.86	0.728	$(31.9 \pm 2.3) \times 10^{-5}$	44.2×10^{-4}	1.23×10^{-4}	6.83×10^{-4}	2.44×10^{-4}	38.6	214	76.9
6.86 - 8.60	0.899	$(19.5 \pm 1.5) \times 10^{-4}$	24.0×10^{-4}	4.51×10^{-4}	3.22×10^{-3}	1.29×10^{-3}	23.2	350	66.7
8.60 - 10.73	1.10	$(58.5 \pm 3.3) \times 10^{-4}$	90.5×10^{-4}	3.20×10^{-3}	5.25×10^{-3}	3.87×10^{-3}	54.8	90.0	66.5
10.73 - 13.34	1.35	$(85.7 \pm 3.1) \times 10^{-4}$	117×10^{-4}	3.13×10^{-3}	1.01×10^{-3}	1.63×10^{-3}	36.5	12.3	19.4
13.34 - 16.55	1.66	$(72.1 \pm 2.1) \times 10^{-4}$	77.8×10^{-4}	5.74×10^{-4}	6.88×10^{-5}	1.36×10^{-5}	7.96	3.06	3.47
16.55 - 20.48	2.03	$(44.4 \pm 1.5) \times 10^{-4}$	45.9×10^{-4}	1.55×10^{-4}	3.88×10^{-6}	7.89×10^{-6}	3.49	3.38	3.38
20.48 - 25.29	2.48	$(255 \pm 9.8) \times 10^{-5}$	267×10^{-5}	1.16×10^{-4}	2.12×10^{-7}	43.2×10^{-7}	4.54	3.84	3.84
25.29 - 31.20	3.05	$(144 \pm 6.8) \times 10^{-5}$	154×10^{-5}	9.62×10^{-5}	1.13×10^{-8}	2.30×10^{-8}	6.68	4.72	4.72
31.20 - 38.43	3.73	$(80.5 \pm 4.5) \times 10^{-5}$	88.1×10^{-5}	7.63×10^{-5}	5.94×10^{-10}	1.21×10^{-10}	9.48	5.59	5.59
38.43 - 47.30	4.58	$(48.2 \pm 2.5) \times 10^{-5}$	50.4×10^{-5}	2.19×10^{-5}	3.10×10^{-11}	6.30×10^{-11}	4.53	5.19	5.19
47.30 - 58.16	5.61	$(28.7 \pm 1.8) \times 10^{-5}$	28.7×10^{-5}	2.26×10^{-7}	2.00×10^{-12}	3.00×10^{-12}	0.0789	6.27	6.27
58.16 - 71.48	6.88	$(15.6 \pm 1.2) \times 10^{-5}$	16.3×10^{-5}	7.34×10^{-6}	1.00×10^{-12}	0	4.70	7.69	7.69
71.48 - 87.79	8.42	$(81.5 \pm 6.4) \times 10^{-6}$	92.7×10^{-6}	1.12×10^{-5}	0	0	13.7	7.85	7.85
87.79 - 107.78	10.3	$(46.6 \pm 4.8) \times 10^{-6}$	52.5×10^{-6}	5.94×10^{-6}	0	0	12.7	10.3	10.3
107.78 - 132.27	12.6	$(26.9 \pm 7.3) \times 10^{-6}$	29.7×10^{-6}	2.84×10^{-6}	0	0	10.5	27.1	27.1
132.27 - 162.29	15.5	$(15.2 \pm 5.2) \times 10^{-6}$	16.8×10^{-6}	1.61×10^{-6}	0	0	10.6	34.2	34.2
162.29 - 199.06	19.0	$(9.10 \pm 2.3) \times 10^{-6}$	9.50×10^{-6}	3.96×10^{-7}	0	0	4.35	25.3	25.3

$0.4 \leq \theta\,\mathrm{m} \leq 0.5$ rad ($\sim 22.9^\circ \leq \theta\,\mathrm{m} \leq \sim 28.6^\circ$)

Bin (GeV)	η (%)	Data	Model	δF_i	δ F$_{i+}$	δ F$_{i-}$	δ F$_{i}$%	δ F$_{i+}$%	δ F$_{i-}$%
0.07 - 0.10	-	-	-	-	-	-	-	-	-
0.10 - 0.15	-	-	-	-	-	-	-	-	-
0.15 - 0.22	-	-	-	-	-	-	-	-	-
0.22 - 0.31	-	-	-	-	-	-	-	-	-
0.31 - 0.44	-	-	-	-	-	-	-	-	-
0.44 - 0.62	-	-	-	-	-	-	-	-	-
0.62 - 0.85	-	-	-	-	-	-	-	-	-
0.85 - 1.15	-	-	-	-	-	-	-	-	-
1.15 - 1.54	-	-	-	-	-	-	-	-	-
1.54 - 2.02	-	-	-	-	-	-	-	-	-
2.02 - 2.62	-	-	-	-	-	-	-	-	-
2.62 - 3.38	-	-	-	-	-	-	-	-	-
3.38 - 4.31	-	-	-	-	-	-	-	-	-
4.31 - 5.45	0.585	$(58.5 \pm 5.9) \times 10^{-5}$	60.5×10^{-5}	2.03×10^{-5}	1.44×10^{-3}	4.00×10^{-4}	4.24	247	69.1
5.45 - 6.86	0.724	$(32.1 \pm 3.0) \times 10^{-4}$	32.2×10^{-5}	8.94×10^{-6}	6.60×10^{-3}	2.09×10^{-3}	4.24	1131	362
6.86 - 8.60	0.893	$(96.2 \pm 6.4) \times 10^{-4}$	128×10^{-4}	3.27×10^{-3}	1.13×10^{-2}	7.27×10^{-3}	6.20	118	75.9
8.60 - 10.73	1.09	$(128 \pm 5.4) \times 10^{-4}$	189×10^{-4}	6.14×10^{-3}	2.50×10^{-3}	4.63×10^{-3}	3.65	26.0	36.4
10.73 - 13.34	1.34	$(115 \pm 2.8) \times 10^{-4}$	132×10^{-4}	1.69×10^{-3}	1.83×10^{-4}	4.81×10^{-4}	32.8	2.91	4.84
13.34 - 16.55	1.65	$(75.6 \pm 2.5) \times 10^{-4}$	78.8×10^{-4}	3.22×10^{-4}	1.07×10^{-5}	2.35×10^{-4}	17.0	3.31	4.54
16.55 - 20.48	2.02	$(45.2 \pm 1.8) \times 10^{-4}$	46.0×10^{-4}	8.05×10^{-5}	5.92×10^{-7}	2.94×10^{-5}	0.513	3.98	4.03
20.48 - 25.29	2.47	$(248 \pm 9.6) \times 10^{-5}$	267×10^{-5}	1.86×10^{-4}	3.22×10^{-8}	1.64×10^{-6}	4.50	3.87	3.87
25.29 - 31.20	3.03	$(142 \pm 6.7) \times 10^{-5}$	154×10^{-5}	1.16×10^{-4}	1.72×10^{-9}	8.93×10^{-8}	4.49	4.72	4.72
31.20 - 38.43	3.71	$(80.0 \pm 4.3) \times 10^{-5}$	88.1×10^{-5}	8.13×10^{-5}	9.00×10^{-11}	4.76×10^{-9}	11.3	5.38	5.38
38.43 - 47.30	4.55	$(48.2 \pm 3.0) \times 10^{-5}$	50.4×10^{-5}	2.19×10^{-5}	4.00×10^{-12}	2.50×10^{-10}	3.04	6.22	6.22
47.30 - 58.16	5.58	$(28.4 \pm 1.8) \times 10^{-5}$	28.7×10^{-5}	3.23×10^{-6}	0	1.30×10^{-11}	0.429	6.34	6.34
58.16 - 71.48	6.84	$(154 \pm 8.8) \times 10^{-6}$	163×10^{-6}	9.34×10^{-6}	0	0	6.06	5.71	5.71
71.48 - 87.79	8.37	$(80.2 \pm 5.9) \times 10^{-6}$	92.7×10^{-6}	1.26×10^{-5}	0	0	16.5	7.36	7.36
87.79 - 107.78	10.3	$(45.8 \pm 2.8) \times 10^{-6}$	52.5×10^{-6}	6.74×10^{-6}	0	0	16.8	6.11	6.11
107.78 - 132.27	12.6	$(26.4 \pm 6.2) \times 10^{-6}$	29.7×10^{-6}	3.34×10^{-6}	0	0	15.7	23.5	23.5
132.27 - 162.29	15.4	$(14.9 \pm 7.9) \times 10^{-6}$	16.8×10^{-6}	1.91×10^{-6}	0	0	17.6	53.0	53.0
162.29 - 199.06	18.9	$(8.9 \pm 1.8) \times 10^{-6}$	9.49×10^{-6}	5.96×10^{-7}	0	0	41.7	20.2	20.2

$0.5 \leq \theta\mathrm{m} \leq 0.6$ rad ($\sim$28.6° $\theta\mathrm{m} \leq \sim$34.4°)

Bin (GeV)	η (%)	Data	Model	δ F$_i$	δ F$_{i+}$	δ F$_{i-}$	δ F$_{i\%}$	δ F$_{i+\%}$	δ F$_{i-\%}$
0.07 - 0.10	-	-	-	-	-	-	-	-	-
0.10 - 0.15	-	-	-	-	-	-	-	-	-
0.15 - 0.22	-	-	-	-	-	-	-	-	-
0.22 - 0.31	-	-	-	-	-	-	-	-	-
0.31 - 0.44	-	-	-	-	-	-	-	-	-
0.44 - 0.62	-	-	-	-	-	-	-	-	-
0.62 - 0.85	-	-	-	-	-	-	-	-	-
0.85 - 1.15	-	-	-	-	-	-	-	-	-
1.15 - 1.54	-	-	-	-	-	-	-	-	-
1.54 - 2.02	-	-	-	-	-	-	-	-	-
2.02 - 2.62	-	-	-	-	-	-	-	-	-
2.62 - 3.38	0.387	$(29.0 \pm 1.4) \times 10^{-5}$	29.4×10^{-5}	4.08×10^{-6}	1.10×10^{-3}	2.17×10^{-4}	1.41	377	76.3
3.38 - 4.31	0.473	$(10.7 \pm 1.1) \times 10^{-4}$	15.4×10^{-4}	4.71×10^{-4}	5.98×10^{-3}	6.84×10^{-4}	44.0	515	108
4.31 - 5.45	0.580	$(62.9 \pm 6.4) \times 10^{-4}$	77.6×10^{-4}	1.47×10^{-3}	2.22×10^{-2}	4.24×10^{-3}	23.3	331	91.3
5.45 - 6.86	0.718	$(18.4 \pm 1.4) \times 10^{-3}$	26.7×10^{-3}	8.34×10^{-3}	3.02×10^{-2}	8.57×10^{-3}	45.3	119	92.3
6.86 - 8.60	0.886	$(23.2 \pm 1.2) \times 10^{-3}$	33.2×10^{-3}	9.89×10^{-3}	1.35×10^{-2}	9.08×10^{-4}	42.4	16.1	38.9
8.60 - 10.73	1.08	$(193 \pm 5.1) \times 10^{-4}$	224×10^{-4}	3.05×10^{-3}	3.30×10^{-3}	2.14×10^{-3}	15.8	2.95	5.41
10.73 - 13.34	1.33	$(128 \pm 3.7) \times 10^{-4}$	134×10^{-4}	6.28×10^{-4}	6.43×10^{-4}	5.71×10^{-4}	4.91	2.89	2.93
13.34 - 16.55	1.63	$(75.6 \pm 2.7) \times 10^{-4}$	79.0×10^{-4}	3.36×10^{-4}	3.37×10^{-4}	3.33×10^{-4}	4.45	3.57	3.57
16.55 - 20.48	2.00	$(43.3 \pm 1.2) \times 10^{-4}$	46.0×10^{-4}	2.71×10^{-4}	2.71×10^{-4}	2.71×10^{-4}	6.26	2.77	2.77
20.48 - 25.29	2.45	$(24.0 \pm 1.0) \times 10^{-4}$	2.67×10^{-4}	2.66×10^{-4}	2.66×10^{-4}	2.66×10^{-4}	11.1	4.17	4.17
25.29 - 31.20	3.01	$(138 \pm 5.6) \times 10^{-5}$	1.54×10^{-4}	1.56×10^{-4}	1.56×10^{-4}	1.56×10^{-4}	11.3	4.06	4.06
31.20 - 38.43	3.68	$(77.1 \pm 4.3) \times 10^{-5}$	88.1×10^{-5}	1.10×10^{-4}	1.10×10^{-4}	1.10×10^{-4}	14.3	5.58	5.58
38.43 - 47.30	4.52	$(47.1 \pm 2.7) \times 10^{-5}$	50.4×10^{-5}	3.29×10^{-5}	3.29×10^{-5}	3.29×10^{-5}	6.98	5.73	5.73
47.30 - 58.16	5.53	$(27.7 \pm 1.8) \times 10^{-5}$	28.7×10^{-5}	1.02×10^{-5}	1.02×10^{-5}	1.02×10^{-5}	3.69	6.50	6.50
58.16 - 71.48	6.78	$(149 \pm 9.9) \times 10^{-6}$	163×10^{-6}	1.43×10^{-5}	1.43×10^{-5}	1.43×10^{-5}	9.62	6.64	6.64
71.48 - 87.79	8.30	$(76.7 \pm 5.1) \times 10^{-6}$	92.7×10^{-6}	1.60×10^{-5}	1.60×10^{-5}	1.60×10^{-5}	20.9	6.65	6.65
87.79 - 107.78	10.2	$(43.4 \pm 2.6) \times 10^{-6}$	52.5×10^{-6}	9.14×10^{-6}	9.14×10^{-6}	9.14×10^{-6}	21.1	5.99	5.99
107.78 - 132.27	12.5	$(24.8 \pm 4.6) \times 10^{-6}$	29.7×10^{-6}	4.94×10^{-6}	4.94×10^{-6}	4.94×10^{-6}	19.9	18.5	18.5
132.27 - 162.29	15.3	$(13.8 \pm 6.3) \times 10^{-6}$	1.68×10^{-6}	3.01×10^{-6}	3.01×10^{-6}	3.01×10^{-6}	21.8	45.7	45.7
162.29 - 199.06	18.7	$(82.1 \pm 6.2) \times 10^{-7}$	9.50×10^{-7}	1.29×10^{-6}	1.29×10^{-6}	1.29×10^{-6}	15.7	7.55	7.55

$0.6 \leq \theta\,\mathrm{m} \leq 0.7$ rad ($\sim 34.4° \leq \theta\,\mathrm{m} \leq \sim 40.1°$)

Bin (GeV)	η (%)	Data	Model	δ F$_i$	δ F$_{i+}$	δ F$_{i-}$	δ F$_{i\%}$	δ F$_{i+\%}$	δ F$_{i-\%}$
0.07 - 0.10	-	-	-	-	-	-	-	-	-
0.10 - 0.15	-	-	-	-	-	-	-	-	-
0.15 - 0.22	-	-	-	-	-	-	-	-	-
0.22 - 0.31	-	-	-	-	-	-	-	-	-
0.31 - 0.44	-	-	-	-	-	-	-	-	-
0.44 - 0.62	-	-	-	-	-	-	-	-	-
0.62 - 0.85	-	-	-	-	-	-	-	-	-
0.85 - 1.15	-	-	-	-	-	-	-	-	-
1.15 - 1.54	-	-	-	-	-	-	-	-	-
1.54 - 2.02	-	-	-	-	-	-	-	-	-
2.02 - 2.62	0.305	$(77.7 \pm 8.3) \times 10^{-5}$	156×10^{-5}	7.82×10^{-4}	8.84×10^{-3}	1.28×10^{-3}	100.6	1137	165
2.62 - 3.38	0.386	$(49.1 \pm 5.9) \times 10^{-4}$	76.4×10^{-4}	2.73×10^{-3}	3.66×10^{-2}	6.26×10^{-3}	55.7	745	128
3.38 - 4.31	0.472	$(27.9 \pm 2.9) \times 10^{-3}$	33.0×10^{-3}	5.13×10^{-3}	6.91×10^{-2}	2.60×10^{-2}	18.	248	93.7
4.31 - 5.45	0.579	$(56.4 \pm 4.0) \times 10^{-3}$	69.6×10^{-3}	1.32×10^{-2}	2.49×10^{-2}	4.10×10^{-2}	23.3	44.7	73.1
5.45 - 6.86	0.716	$(52.6 \pm 1.7) \times 10^{-3}$	59.3×10^{-3}	6.75×10^{-3}	2.50×10^{-3}	1.07×10^{-2}	12.8	5.74	20.6
6.86 - 8.60	0.883	$(35.6 \pm 1.2) \times 10^{-3}$	37.6×10^{-3}	2.04×10^{-3}	8.90×10^{-4}	1.68×10^{-4}	5.74	3.40	4.20
8.60 - 10.73	1.08	$(212 \pm 9.0) \times 10^{-4}$	227×10^{-4}	1.46×10^{-3}	5.60×10^{-5}	1.03×10^{-5}	6.89	4.25	4.25
10.73 - 13.34	1.32	$(129 \pm 5.3) \times 10^{-4}$	134×10^{-4}	5.46×10^{-4}	6.10×10^{-7}	3.32×10^{-6}	4.24	4.11	4.11
13.34 - 16.55	1.63	$(75.8 \pm 3.3) \times 10^{-4}$	79.0×10^{-4}	3.17×10^{-4}	3.48×10^{-8}	1.89×10^{-7}	4.18	4.35	4.35
16.55 - 20.48	1.99	$(41.7 \pm 1.5) \times 10^{-4}$	46.0×10^{-4}	4.31×10^{-4}	1.92×10^{-9}	1.05×10^{-8}	10.3	3.60	3.60
20.48 - 25.29	2.44	$(24.9 \pm 1.1) \times 10^{-4}$	26.7×10^{-4}	1.76×10^{-4}	1.00×10^{-10}	5.70×10^{-10}	7.07	4.42	4.42
25.29 - 31.20	3.00	$(134 \pm 5.6) \times 10^{-5}$	153×10^{-5}	1.96×10^{-4}	0	1.00×10^{-12}	14.6	4.18	4.18
31.20 - 38.43	3.67	$(75.1 \pm 4.0) \times 10^{-5}$	8.81×10^{-5}	1.30×10^{-4}	0	0	17.3	5.33	5.33
38.43 - 47.30	4.50	$(46.0 \pm 2.7) \times 10^{-5}$	50.4×10^{-5}	4.39×10^{-5}	0	0	9.53	5.87	5.87
47.30 - 58.16	5.51	$(27.0 \pm 1.8) \times 10^{-5}$	28.7×10^{-5}	1.72×10^{-5}	0	0	6.38	6.67	6.67
58.16 - 71.48	6.76	$(14.6 \pm 1.2) \times 10^{-5}$	16.3×10^{-5}	1.73×10^{-5}	0	0	11.9	8.22	8.22
71.48 - 87.79	8.28	$(76.0 \pm 4.6) \times 10^{-6}$	92.7×10^{-6}	1.67×10^{-5}	0	0	22.0	6.05	6.05
87.79 - 107.78	10.1	$(43.5 \pm 5.8) \times 10^{-6}$	52.5×10^{-6}	9.04×10^{-6}	0	0	20.8	13.3	13.3
107.78 - 132.27	12.4	$(25.2 \pm 4.5) \times 10^{-6}$	29.7×10^{-6}	4.54×10^{-6}	0	0	18.0	17.9	17.9
132.27 - 162.29	15.2	$(14.3 \pm 3.9) \times 10^{-6}$	16.8×10^{-6}	2.51×10^{-6}	0	0	17.6	27.3	27.3
162.29 - 199.06	18.7	$(8.6 \pm 1.5) \times 10^{-6}$	9.5×10^{-6}	8.96×10^{-7}	0	0	10.4	17.4	17.4

$0.7 \leq \theta\mathrm{m} \leq 0.8$ rad ($\sim 40.1^\circ \leq \theta\mathrm{m} \leq \sim 45.8^\circ$)

Bin (GeV)	η (%)	Data	Model	δ F$_i$	δ F$_{i+}$	δ F$_{i-}$	δ F$_{i\%}$	δ F$_{i+\%}$	δ F$_{i-\%}$
0.07 - 0.10	-	-	-	-	-	-	-	-	-
0.10 - 0.15	-	-	-	-	-	-	-	-	-
0.15 - 0.22	-	-	-	-	-	-	-	-	-
0.22 - 0.31	-	-	-	-	-	-	-	-	-
0.31 - 0.44	-	-	-	-	-	-	-	-	-
0.44 - 0.62	-	-	-	-	-	-	-	-	-
0.62 - 0.85	-	-	-	-	-	-	-	-	-
0.85 - 1.15	-	-	-	-	-	-	-	-	-
1.15 - 1.54	-	-	-	-	-	-	-	-	-
1.54 - 2.02	0.243	$(44.8 \pm 6.7) \times 10^{-4}$	185×10^{-4}	1.40×10^{-2}	1.28×10^{-1}	1.62×10^{-2}	312	2850	362
2.02 - 2.62	0.304	$(43.1 \pm 5.8) \times 10^{-3}$	72.3×10^{-3}	2.92×10^{-2}	1.94×10^{-1}	6.19×10^{-2}	67.7	451	144
2.62 - 3.38	0.385	$(11.4 \pm 1.1) \times 10^{-2}$	16.0×10^{-2}	4.57×10^{-2}	7.50×10^{-2}	1.15×10^{-1}	40.1	66.5	102
3.38 - 4.31	0.471	$(124 \pm 4.6) \times 10^{-3}$	149×10^{-3}	2.53×10^{-2}	8.95×10^{-3}	4.72×10^{-2}	20.4	8.12	38.2
4.31 - 5.45	0.577	$(88.4 \pm 4.3) \times 10^{-3}$	99.9×10^{-3}	1.15×10^{-2}	7.03×10^{-4}	5.40×10^{-3}	13.0	4.93	7.81
5.45 - 6.86	0.714	$(55.6 \pm 3.2) \times 10^{-3}$	62.2×10^{-3}	6.64×10^{-3}	4.87×10^{-5}	3.95×10^{-4}	11.9	5.76	5.80
6.86 - 8.60	0.881	$(34.0 \pm 1.8) \times 10^{-3}$	37.8×10^{-3}	3.84×10^{-3}	3.13×10^{-6}	2.55×10^{-5}	11.3	5.29	5.29
8.60 - 10.73	1.08	$(20.2 \pm 1.1) \times 10^{-3}$	22.7×10^{-3}	2.47×10^{-3}	1.91×10^{-7}	1.56×10^{-6}	12.2	5.45	5.45
10.73 - 13.34	1.32	$(121 \pm 6.4) \times 10^{-4}$	13.4×10^{-4}	1.35×10^{-3}	1.12×10^{-8}	9.21×10^{-8}	11.1	5.29	5.29
13.34 - 16.55	1.63	$(69.0 \pm 3.8) \times 10^{-4}$	79.0×10^{-4}	9.97×10^{-4}	6.40×10^{-10}	5.25×10^{-9}	14.5	5.51	5.51
16.55 - 20.48	1.99	$(40.5 \pm 2.1) \times 10^{-4}$	46.0×10^{-4}	5.51×10^{-4}	4.00×10^{-11}	2.90×10^{-10}	13.6	5.19	5.19
20.48 - 25.29	2.44	$(22.7 \pm 1.3) \times 10^{-4}$	2.67×10^{-4}	3.96×10^{-4}	0	2.00×10^{-11}	17.5	5.73	5.73
25.29 - 31.20	2.99	$(132 \pm 8.7) \times 10^{-5}$	154×10^{-5}	2.16×10^{-4}	0	0	16.4	6.59	6.59
31.20 - 38.43	3.66	$(69.2 \pm 4.5) \times 10^{-5}$	88.1×10^{-5}	1.89×10^{-4}	0	0	27.4	6.50	6.50
38.43 - 47.30	4.49	$(44.7 \pm 2.8) \times 10^{-5}$	50.4×10^{-5}	5.69×10^{-5}	0	0	12.7	6.26	6.26
47.30 - 58.16	5.50	$(26.3 \pm 1.9) \times 10^{-5}$	28.7×10^{-5}	2.42×10^{-5}	0	0	9.21	7.22	7.22
58.16 - 71.48	6.74	$(142 \pm 9.9) \times 10^{-6}$	16.3×10^{-6}	2.13×10^{-5}	0	0	15.0	6.97	6.97
71.48 - 87.79	8.26	$(72.9 \pm 4.5) \times 10^{-6}$	92.7×10^{-6}	1.98×10^{-5}	0	0	27.2	6.17	6.17
87.79 - 107.78	10.1	$(41.5 \pm 3.0) \times 10^{-6}$	52.5×10^{-6}	1.10×10^{-5}	0	0	26.6	7.23	7.23
107.78 - 132.27	12.4	$(23.9 \pm 4.4) \times 10^{-6}$	29.7×10^{-6}	5.84×10^{-6}	0	0	24.4	18.4	18.4
132.27 - 162.29	15.2	$(13.4 \pm 4.7) \times 10^{-6}$	16.8×10^{-6}	3.41×10^{-6}	0	0	25.5	35.1	35.1
162.29 - 199.06	18.6	$(80.6 \pm 4.3) \times 10^{-7}$	95.0×10^{-7}	1.44×10^{-6}	0	0	17.8	5.33	5.33

$0.8 \leq \theta \mathrm{m} \leq 0.9$ rad ($\sim 45.8^\circ \leq \theta \mathrm{m} \leq \sim 51.6^\circ$)

Bin (GeV)	η (%)	Data	Model	δ F$_i$	δ F$_{i+}$	δ F$_{i-}$	δ F$_{i}$%	δ F$_{i+}$%	δ F$_{i-}$%
0.07 - 0.10	-	-	-	-	-	-	-	-	-
0.10 - 0.15	-	-	-	-	-	-	-	-	-
0.15 - 0.22	-	-	-	-	-	-	-	-	-
0.22 - 0.31	-	-	-	-	-	-	-	-	-
0.31 - 0.44	-	-	-	-	-	-	-	-	-
0.44 - 0.62	-	-	-	-	-	-	-	-	-
0.62 - 0.85	-	-	-	-	-	-	-	-	-
0.85 - 1.15	0.151	$(60.9 \pm 6.5) \times 10^{-3}$	127×10^{-3}	9.19×10^{-2}	5.82×10^{-1}	1.16×10^{-1}	263	1669	333
1.15 - 1.54	0.197	$(23.7 \pm 2.9) \times 10^{-2}$	33.4×10^{-2}	1.80×10^{-1}	3.61×10^{-1}	2.91×10^{-1}	117	235	190
1.54 - 2.02	0.242	$(44.8 \pm 6.7) \times 10^{-2}$	44.7×10^{-2}	1.66×10^{-1}	8.28×10^{-2}	3.01×10^{-1}	59.2	31.7	108
2.02 - 2.62	0.303	$(43.1 \pm 5.8) \times 10^{-2}$	36.1×10^{-2}	5.18×10^{-2}	9.95×10^{-3}	9.44×10^{-2}	16.8	6.66	31.8
2.62 - 3.38	0.383	$(11.4 \pm 1.1) \times 10^{-2}$	24.6×10^{-2}	2.00×10^{-2}	8.97×10^{-4}	1.13×10^{-2}	8.86	6.21	7.95
3.38 - 4.31	0.469	$(124 \pm 4.6) \times 10^{-2}$	15.9×10^{-2}	5.22×10^{-3}	7.09×10^{-5}	9.30×10^{-4}	3.39	7.14	7.17
4.31 - 5.45	0.575	$(88.4 \pm 4.3) \times 10^{-3}$	101×10^{-3}	5.33×10^{-3}	5.24×10^{-6}	6.91×10^{-5}	5.59	6.19	6.19
5.45 - 6.86	0.711	$(55.6 \pm 3.2) \times 10^{-3}$	62.3×10^{-3}	2.99×10^{-3}	3.60×10^{-7}	4.75×10^{-6}	5.05	5.90	5.90
6.86 - 8.60	0.878	$(34.0 \pm 1.8) \times 10^{-3}$	37.8×10^{-3}	1.54×10^{-3}	2.30×10^{-8}	3.05×10^{-7}	4.24	7.16	7.16
8.60 - 10.73	1.07	$(20.2 \pm 1.1) \times 10^{-3}$	22.7×10^{-3}	8.73×10^{-4}	1.40×10^{-9}	1.86×10^{-8}	4.00	7.34	7.34
10.73 - 13.34	1.32	$(121 \pm 6.4) \times 10^{-4}$	13.4×10^{-4}	6.47×10^{-4}	1.00×10^{-10}	1.10×10^{-9}	5.06	6.25	6.25
13.34 - 16.55	1.62	$(69.0 \pm 3.8) \times 10^{-4}$	79.0×10^{-4}	3.77×10^{-4}	1.00×10^{-11}	6.00×10^{-12}	5.02	5.72	5.72
16.55 - 20.48	1.98	$(40.5 \pm 2.1) \times 10^{-4}$	46.0×10^{-4}	5.81×10^{-4}	0	0	14.5	7.46	7.46
20.48 - 25.29	2.43	$(22.7 \pm 1.3) \times 10^{-5}$	26.6×10^{-5}	2.96×10^{-4}	0	0	12.5	3.38	3.38
25.29 - 31.20	2.98	$(132 \pm 8.7) \times 10^{-5}$	15.4×10^{-5}	2.66×10^{-4}	0	0	21.0	5.04	5.04
31.20 - 38.43	3.65	$(69.2 \pm 4.5) \times 10^{-5}$	88.1×10^{-5}	2.66×10^{-4}	0	0	43.3	9.27	9.27
38.43 - 47.30	4.48	$(44.7 \pm 2.8) \times 10^{-5}$	50.4×10^{-5}	6.39×10^{-5}	0	0	14.5	7.95	7.95
47.30 - 58.16	5.48	$(26.3 \pm 1.9) \times 10^{-5}$	28.7×10^{-5}	3.02×10^{-5}	0	0	11.8	10.9	10.9
58.16 - 71.48	6.72	$(142 \pm 9.9) \times 10^{-5}$	16.3×10^{-5}	2.43×10^{-5}	0	0	17.5	9.35	9.35
71.48 - 87.79	8.23	$(72.9 \pm 4.5) \times 10^{-6}$	92.7×10^{-6}	2.10×10^{-5}	0	0	29.3	8.93	8.93
87.79 - 107.78	10.1	$(41.5 \pm 3.0) \times 10^{-6}$	52.5×10^{-6}	1.14×10^{-5}	0	0	27.8	9.98	9.98
107.78 - 132.27	12.4	$(23.9 \pm 4.4) \times 10^{-6}$	29.7×10^{-6}	5.84×10^{-6}	0	0	24.4	18.4	18.4
132.27 - 162.29	15.1	$(13.6 \pm 6.5) \times 10^{-6}$	16.8×10^{-6}	3.21×10^{-6}	0	0	23.6	47.8	47.8
162.29 - 199.06	18.6	$(8.2 \pm 1.3) \times 10^{-6}$	9.5×10^{-6}	1.30×10^{-6}	0	0	15.8	15.9	15.9

$0.9 \leq \theta\mathrm{m} \leq 1.0$ rad ($\sim 51.6^\circ \leq \theta\mathrm{m} \leq \sim 57.3^\circ$)

Bin (GeV)	η (%)	Data	Model	δ F$_i$	δ F$_{i+}$	δ F$_{i-}$	δ F$_{i\%}$	δ F$_{i+\%}$	δ F$_{i-\%}$
0.07 - 0.10	-	-	-	-	-	-	-	-	-
0.10 - 0.15	-	-	-	-	-	-	-	-	-
0.15 - 0.22	-	-	-	-	-	-	-	-	-
0.22 - 0.31	-	-	-	-	-	-	-	-	-
0.31 - 0.44	0.0653	$(29.3 \pm 7.1) \times 10^{-2}$	77.3×10^{-2}	4.80×10^{-1}	6.42×10^{-1}	7.08×10^{-1}	164	221	243
0.44 - 0.62	0.0905	$(4.7 \pm 1.1) \times 10^{-1}$	10.8×10^{-1}	6.09×10^{-1}	2.87×10^{-1}	8.99×10^{-1}	129	65.3	193
0.62 - 0.85	0.116	$(7.5 \pm 1.3) \times 10^{-1}$	11.2×10^{-1}	3.72×10^{-1}	7.77×10^{-2}	6.82×10^{-1}	49.6	20.2	92.5
0.85 - 1.15	0.151	$(85.3 \pm 7.5) \times 10^{-2}$	96.3×10^{-2}	1.10×10^{-1}	1.46×10^{-2}	2.53×10^{-1}	12.9	8.96	31.0
1.15 - 1.54	0.196	$(71.7 \pm 4.5) \times 10^{-2}$	74.1×10^{-2}	2.40×10^{-2}	2.06×10^{-3}	4.60×10^{-2}	3.35	6.28	8.97
1.54 - 2.02	0.241	$(52.4 \pm 4.5) \times 10^{-2}$	53.6×10^{-2}	1.18×10^{-2}	2.40×10^{-4}	5.68×10^{-3}	2.26	8.59	8.66
2.02 - 2.62	0.302	$(36.2 \pm 2.9) \times 10^{-2}$	37.1×10^{-2}	9.30×10^{-3}	2.46×10^{-5}	5.87×10^{-4}	2.57	8.01	8.01
2.62 - 3.38	0.382	$(24.8 \pm 2.1) \times 10^{-2}$	24.7×10^{-2}	1.02×10^{-3}	2.16×10^{-6}	5.16×10^{-5}	0.411	8.47	8.47
3.38 - 4.31	0.468	$(16.2 \pm 1.1) \times 10^{-2}$	15.9×10^{-2}	2.70×10^{-3}	1.70×10^{-7}	4.07×10^{-6}	1.67	6.79	6.79
4.31 - 5.45	0.573	$(103 \pm 7.7) \times 10^{-3}$	10.1×10^{-3}	2.37×10^{-3}	1.20×10^{-8}	3.00×10^{-7}	2.30	7.48	7.48
5.45 - 6.86	0.709	$(63.8 \pm 5.0) \times 10^{-3}$	62.3×10^{-3}	1.51×10^{-3}	9.00×10^{-10}	2.06×10^{-8}	2.36	7.84	7.84
6.86 - 8.60	0.875	$(39.0 \pm 2.8) \times 10^{-3}$	37.8×10^{-3}	1.16×10^{-3}	1.00×10^{-10}	1.30×10^{-9}	2.98	7.18	7.18
8.60 - 10.73	1.07	$(22.5 \pm 1.6) \times 10^{-3}$	22.7×10^{-3}	1.73×10^{-4}	0	1.00×10^{-10}	0.768	7.11	7.11
10.73 - 13.34	1.31	$(14.1 \pm 1.3) \times 10^{-3}$	13.4×10^{-3}	6.53×10^{-4}	0	0	4.63	9.22	9.22
13.34 - 16.55	1.61	$(78.0 \pm 5.7) \times 10^{-4}$	79.0×10^{-4}	9.71×10^{-5}	0	0	1.25	7.31	7.31
16.55 - 20.48	1.98	$(39.3 \pm 3.3) \times 10^{-4}$	46.0×10^{-4}	6.71×10^{-4}	0	0	17.1	8.40	8.40
20.48 - 25.29	2.42	$(23.8 \pm 2.0) \times 10^{-4}$	26.7×10^{-4}	2.86×10^{-4}	0	0	12.0	8.40	8.40
25.29 - 31.20	2.97	$(12.3 \pm 1.4) \times 10^{-4}$	15.4×10^{-4}	3.06×10^{-4}	0	0	24.9	11.4	11.4
31.20 - 38.43	3.63	$(78.0 \pm 8.8) \times 10^{-5}$	88.1×10^{-5}	1.01×10^{-4}	0	0	13.0	11.3	11.3
38.43 - 47.30	4.46	$(44.1 \pm 4.6) \times 10^{-5}$	50.4×10^{-5}	6.29×10^{-5}	0	0	14.3	10.4	10.4
47.30 - 58.16	5.46	$(27.0 \pm 2.6) \times 10^{-5}$	28.7×10^{-5}	1.72×10^{-5}	0	0	6.38	9.63	9.63
58.16 - 71.48	6.70	$(14.3 \pm 1.5) \times 10^{-5}$	16.3×10^{-5}	2.03×10^{-5}	0	0	14.2	10.5	10.5
71.48 - 87.79	8.20	$(72.5 \pm 6.5) \times 10^{-6}$	92.7×10^{-6}	2.02×10^{-5}	0	0	27.9	8.97	8.97
87.79 - 107.78	10.0	$(40.3 \pm 6.3) \times 10^{-6}$	52.5×10^{-6}	1.22×10^{-5}	0	0	30.4	15.6	15.6
107.78 - 132.27	12.3	$(2.3 \pm 1.2) \times 10^{-5}$	2.97×10^{-5}	6.74×10^{-6}	0	0	29.3	52.2	52.2
132.27 - 162.29	15.1	$(12.3 \pm 8.9) \times 10^{-6}$	16.8×10^{-6}	4.51×10^{-6}	0	0	36.7	72.4	72.4
162.29 - 199.06	18.5	$(7.2 \pm 3.7) \times 10^{-6}$	9.5×10^{-6}	2.30×10^{-6}	0	0	31.9	51.4	51.4

$1.0 \leq \theta$ m ≤ 1.1 rad ($\sim 57.3^\circ \leq \theta$ m $\leq \sim 63.0^\circ$)									
Bin (GeV)	η (%)	Data	Model	δ F$_i$	δ F$_{i+}$	δ F$_{i-}$	δ F$_{i,\%}$	δ F$_{i+\%}$	δ F$_{i-\%}$
0.07 - 0.10	0.0151	(9.20 ± 2.6) ×10^{-1}	8.20×10^{-1}	1.00×10^{-1}	5.45×10^{-3}	2.09×10^{-1}	10.9	28.3	36.3
0.10 - 0.15	0.0251	(9.80 ± 1.2) ×10^{-1}	1.05×10^{-1}	6.55×10^{-2}	4.62×10^{-3}	1.94×10^{-1}	6.68	12.3	23.3
0.15 - 0.22	0.0352	(109 ± 6.7) ×10^{-2}	126×10^{-2}	1.74×10^{-1}	3.12×10^{-3}	1.43×10^{-1}	15.9	6.15	14.5
0.22 - 0.31	0.0452	(126 ± 5.3) ×10^{-2}	141×10^{-2}	1.47×10^{-1}	1.69×10^{-3}	8.21×10^{-2}	11.7	4.21	7.56
0.31 - 0.44	0.0653	(139 ± 4.1) ×10^{-2}	145×10^{-2}	6.06×10^{-2}	6.98×10^{-4}	3.52×10^{-2}	4.36	2.95	3.89
0.44 - 0.62	0.0905	(132 ± 4.8) ×10^{-2}	138×10^{-2}	5.59×10^{-2}	2.08×10^{-4}	1.07×10^{-2}	4.23	3.64	3.73
0.62 - 0.85	0.116	(114 ± 4.2) ×10^{-2}	120×10^{-2}	6.24×10^{-2}	4.71×10^{-5}	2.43×10^{-3}	5.47	3.68	3.69
0.85 - 1.15	0.151	(92.8 ± 3.2) ×10^{-2}	97.8×10^{-2}	4.97×10^{-2}	8.38×10^{-6}	4.34×10^{-4}	5.35	3.45	3.45
1.15 - 1.54	0.196	(72.4 ± 2.4) ×10^{-2}	74.3×10^{-2}	1.92×10^{-2}	11.7×10^{-6}	6.03×10^{-5}	2.65	3.31	3.31
1.54 - 2.02	0.241	(51.1 ± 1.4) ×10^{-2}	53.6×10^{-2}	2.51×10^{-2}	13.6×10^{-7}	7.03×10^{-6}	4.91	2.74	2.74
2.02 - 2.62	0.302	(37.0 ± 1.1) ×10^{-2}	37.1×10^{-2}	1.32×10^{-3}	14.0×10^{-8}	7.20×10^{-7}	0.358	2.97	2.97
2.62 - 3.38	0.382	(241 ± 6.4) ×10^{-3}	247×10^{-3}	5.98×10^{-3}	1.00×10^{-9}	6.40×10^{-8}	2.48	2.66	2.66
3.38 - 4.31	0.467	(163 ± 3.1) ×10^{-3}	159×10^{-3}	3.70×10^{-3}	0	5.00×10^{-9}	2.27	1.90	1.90
4.31 - 5.45	0.573	(102 ± 2.9) ×10^{-3}	101×10^{-3}	1.37×10^{-3}	0	1.00×10^{-9}	1.34	2.84	2.84
5.45 - 6.86	0.709	(61.4 ± 1.3) ×10^{-3}	62.3×10^{-3}	8.92×10^{-4}	0	0	1.45	2.12	2.12
6.86 - 8.60	0.874	(390 ± 8.2) ×10^{-4}	378×10^{-4}	1.16×10^{-3}	0	0	2.98	2.10	2.10
8.60 - 10.73	1.07	(223 ± 6.5) ×10^{-4}	227×10^{-4}	3.73×10^{-4}	0	0	1.67	2.91	2.91
10.73 0 13.34	1.31	(136 ± 4.5) ×10^{-4}	134×10^{-4}	1.53×10^{-4}	0	0	1.12	3.31	3.31
13.34 - 16.55	1.61	(76.2 ± 2.7) ×10^{-4}	79.0×10^{-4}	2.77×10^{-4}	0	0	3.64	3.54	3.54
16.55 - 20.48	1.97	(39.6 ± 1.3) ×10^{-4}	46.0×10^{-4}	6.41×10^{-4}	0	0	16.2	3.28	3.28
20.48 - 25.29	2.42	(22.0 ± 1.3) ×10^{-4}	26.7×10^{-4}	4.66×10^{-4}	0	0	21.2	5.91	5.91
25.29 - 31.20	2.97	(118 ± 7.9) ×10^{-5}	154×10^{-5}	3.56×10^{-4}	0	0	30.2	6.69	6.69
31.20 - 38.43	3.63	(76.7 ± 6.5) ×10^{-5}	88.1×10^{-5}	1.14×10^{-4}	0	0	14.9	8.47	8.47
38.43 - 47.30	4.46	(47.7 ± 3.7) ×10^{-5}	50.4×10^{-5}	2.69×10^{-5}	0	0	5.63	7.76	7.76
47.30 - 58.16	5.46	(28.5 ± 2.6) ×10^{-5}	28.7×10^{-5}	2.23×10^{-6}	0	0	0.781	9.12	9.12
58.16 - 71.48	6.69	(154 ± 9.8) ×10^{-6}	163×10^{-6}	9.34×10^{-6}	0	0	6.06	6.36	6.36
71.48 - 87.79	8.20	(79.3 ± 8.7) ×10^{-6}	92.7×10^{-6}	1.34×10^{-5}	0	0	16.9	11.0	11.0
87.79 - 107.78	10.0	(44.8 ± 7.9) ×10^{-6}	52.5×10^{-6}	7.74×10^{-6}	0	0	17.3	17.6	17.6
107.78 - 132.27	12.3	(2.6 ± 1.2) ×10^{-5}	2.97×10^{-5}	3.74×10^{-6}	0	0	14.4	46.1	46.1
132.27 - 162.29	15.1	(1.4 ± 1.4) ×10^{-5}	1.68×10^{-5}	2.81×10^{-6}	0	0	20.1	100	100
162.29 - 199.06	18.5	(8.5 ± 2.4) ×10^{-6}	9.5×10^{-6}	9.96×10^{-7}	0	0	11.7	28.2	28.2

Table 3.2: Comparison between the AMS-01's data and the model's estimates according to geomagnetic latitudes θ_m; the parameter η represents the weight associated to each energy bin.
Discrepancies and relative percentile ratios between data and model estimates (average, higher and lowest θ_m considered) are also reported. Unit of measures for fluxes is c s^{-1} m^{-2} sr^{-1} MeV^{-1}.

Appendix B

Comparison with BESS-98, IMAX and CAPRICE data

BESS					
Bin (GeV)	η (%)	Data	Model	δF	δF$_{\%}$ (%)
1.00 - 1.17	0.145	$(8.92 \pm 0.12 \pm 0.22) \times 10^2$	9.55×10^{-2}	6.32×10^{-2}	7.08
1.17 - 1.36	0.162	$(7.72 \pm 0.11 \pm 0.19) \times 10^2$	8.28×10^{-2}	5.56×10^{-2}	7.20
1.36 - 1.58	0.188	$(6.74 \pm 0.09 \pm 0.17) \times 10^2$	7.03×10^{-2}	2.89×10^{-2}	4.28
1.58 - 1.85	0.231	$(5.46 \pm 0.08 \pm 0.14) \times 10^2$	5.87×10^{-2}	4.15×10^{-2}	7.59
1.85 - 2.15	0.256	$(4.52 \pm 0.07 \pm 0.11) \times 10^2$	4.78×10^{-2}	2.64×10^{-2}	5.84
2.15 - 2.51	0.308	$(3.63 \pm 0.05 \pm 0.09) \times 10^2$	3.84×10^{-2}	2.13×10^{-2}	5.87
2.51 - 2.93	0.359	$(2.83 \pm 0.04 \pm 0.07) \times 10^2$	3.04×10^{-2}	2.11×10^{-2}	7.45
2.93 - 3.41	0.410	$(2.22 \pm 0.04 \pm 0.06) \times 10^2$	2.36×10^{-2}	1.35×10^{-2}	6.10
3.41 - 3.98	0.487	$(1.71 \pm 0.03 \pm 0.05) \times 10^2$	1.80×10^{-2}	8.86×10^{-3}	5.18
3.98 - 4.64	0.564	$(1.27 \pm 0.02 \pm 0.03) \times 10^2$	1.34×10^{-2}	7.36×10^{-3}	5.80
4.64 - 5.41	0.658	$(9.65 \pm 0.19 \pm 0.26) \times 10$	9.94×10	2.94×10^{-3}	3.04
5.41 - 6.31	0.769	$(6.89 \pm 0.15 \pm 0.19) \times 10$	7.25×10	3.62×10^{-3}	5.25
6.31 - 7.36	0.897	$(4.91 \pm 0.02 \pm 0.20) \times 10$	5.22×10	3.07×10^{-3}	6.26
7.36 - 8.58	1.04	$(3.43 \pm 0.01 \pm 0.14) \times 10$	3.71×10	2.81×10^{-3}	8.19
8.58 - 10.0	1.21	$(2.42 \pm 0.01 \pm 0.10) \times 10$	2.62×10	1.96×10^{-3}	8.11
10.0 - 11.7	1.45	$(1.70 \pm 0.01 \pm 0.07) \times 10$	1.82×10	1.17×10^{-3}	6.88
11.7 - 13.6	1.62	$(1.18 \pm 0.01 \pm 0.05) \times 10$	1.25×10	7.30×10^{-4}	6.18
13.6 - 15.8	1.88	$8.05 \pm 0.04 \pm 0.33$	8.72	3.69×10^{-4}	4.41
15.8 - 18.5	2.31	$5.57 \pm 0.03 \pm 0.23$	5.87	2.96×10^{-4}	5.31
18.5 - 21.5	2.56	$3.78 \pm 0.03 \pm 0.16$	3.99	2.05×10^{-4}	5.43
21.5 - 25.1	3.08	$2.51 \pm 0.02 \pm 0.10$	2.68	1.70×10^{-4}	6.78
25.1 - 29.3	3.59	$1.67 \pm 0.01 \pm 0.07$	1.78	1.15×10^{-4}	6.87
29.3 - 34.1	4.10	$1.10 \pm 0.01 \pm 0.05$	1.20	9.87×10^{-5}	8.97
34.1 - 39.8	4.87	$(7.35 \pm 0.08 \pm 0.31) \times 10^{-1}$	7.91×10^{-1}	5.64×10^{-5}	7.67
39.8 - 46.4	5.64	$(4.87 \pm 0.06 \pm 0.20) \times 10^{-1}$	5.24×10^{-1}	3.67×10^{-5}	7.53
46.4 - 54.1	6.58	$(3.22 \pm 0.05 \pm 0.14) \times 10^{-1}$	3.46×10^{-1}	2.38×10^{-5}	7.38
54.1 - 63.1	7.69	$(2.10 \pm 0.04 \pm 0.09) \times 10^{-1}$	2.27×10^{-1}	1.75×10^{-5}	8.32
63.1 - 73.6	8.97	$(1.36 \pm 0.03 \pm 0.06) \times 10^{-1}$	1.50×10^{-1}	1.38×10^{-5}	10.1
73.6 - 85.8	10.4	$(9.17 \pm 0.20 \pm 0.39) \times 10^{-2}$	9.77×10^{-2}	6.00×10^{-6}	6.54
85.8 - 100.	12.1	$(6.08 \pm 0.15 \pm 0.26) \times 10^{-2}$	6.36×10^{-2}	2.84×10^{-6}	4.68
100. - 117.	14.5	$(4.00 \pm 0.12 \pm 0.17) \times 10^{-2}$	4.15×10^{-2}	1.54×10^{-6}	3.85

IMAX								
Bin (GeV)	η (%)	Data	Model	δ F$_i$	δ F$_{i+}$	δ F$_{i-}$	δ F$_i$%	δ F$_{i+}$%	δ F$_{i-}$%
0.18 - 0.20	9.62 $\times 10^{-3}$	$(6.51 \pm 0.09 \pm 1.35) \times 10^2$	9.31×10^2	2.80×10^{-1}	13.6×10^{-1}	4.58×10^{-1}	43.0	29.5	73.4
0.20 - 0.23	1.44 $\times 10^{-2}$	$(7.15 \pm 0.08 \pm 1.24) \times 10^2$	9.71×10^2	2.56×10^{-1}	10.8×10^{-1}	4.38×10^{-1}	35.8	23.0	63.7
0.23 - 0.27	1.92 $\times 10^{-2}$	$(8.01 \pm 0.08 \pm 1.07) \times 10^2$	10.3×10^2	2.31×10^{-1}	7.87×10^{-2}	4.17×10^{-1}	28.8	16.6	53.8
0.27 - 0.33	2.88 $\times 10^{-2}$	$(8.45 \pm 0.07 \pm 0.83) \times 10^2$	10.8×10^2	2.35×10^{-1}	8.19×10^{-2}	4.22×10^{-1}	27.9	13.8	50.9
0.33 - 0.40	3.37 $\times 10^{-2}$	$(8.92 \pm 0.06 \pm 0.68) \times 10^2$	11.1×10^2	2.17×10^{-1}	6.61×10^{-2}	3.99×10^{-1}	24.4	10.6	45.4
0.40 - 0.50	4.81 $\times 10^{-2}$	$(8.48 \pm 0.05 \pm 0.57) \times 10^2$	11.1×10^2	2.64×10^{-1}	1.21×10^{-1}	4.34×10^{-1}	31.1	15.8	51.7
0.50 - 0.63	6.25 $\times 10^{-2}$	$(7.93 \pm 0.05 \pm 0.51) \times 10^2$	10.8×10^2	2.84×10^{-1}	1.55×10^{-1}	4.37×10^{-1}	35.9	20.6	55.4
0.63 - 0.80	8.17 $\times 10^{-2}$	$(7.15 \pm 0.04 \pm 0.46) \times 10^2$	9.99×10^2	2.84×10^{-1}	1.73×10^{-1}	4.12×10^{-1}	39.7	25.1	58.0
0.80 - 1.02	1.06 $\times 10^{-1}$	$(6.22 \pm 0.03 \pm 0.39) \times 10^2$	8.79×10^2	2.57×10^{-1}	1.69×10^{-1}	3.58×10^{-1}	41.3	27.8	57.8
1.02 - 1.31	1.39 $\times 10^{-1}$	$(5.19 \pm 0.03 \pm 0.33) \times 10^2$	7.38×10^2	2.19×10^{-1}	1.52×10^{-1}	2.93×10^{-1}	42.1	30.0	56.7
1.31 - 1.68	1.78 $\times 10^{-1}$	$(4.25 \pm 0.02 \pm 0.27) \times 10^2$	5.88×10^2	1.63×10^{-1}	1.17×10^{-1}	2.15×10^{-1}	38.4	28.2	51.0
1.68 - 2.15	2.26 $\times 10^{-1}$	$(3.24 \pm 0.02 \pm 0.21) \times 10^2$	4.43×10^2	1.19×10^{-1}	8.81×10^{-2}	1.52×10^{-1}	36.7	28.0	47.4
2.15 - 2.77	2.98 $\times 10^{-1}$	$(2.37 \pm 0.01 \pm 0.15) \times 10^2$	3.16×10^2	7.93×10^{-2}	6.05×10^{-2}	9.96×10^{-2}	33.5	26.3	42.5
2.77 - 3.56	3.80 $\times 10^{-1}$	$(1.61 \pm 0.01 \pm 0.10) \times 10^2$	2.14×10^2	5.33×10^{-2}	4.26×10^{-2}	6.49×10^{-2}	33.1	27.2	40.8
3.56 - 4.59	4.95 $\times 10^{-1}$	$(1.05 \pm 0.01 \pm 0.07) \times 10^2$	1.39×10^2	3.36×10^{-2}	2.78×10^{-2}	3.98×10^{-2}	32.0	27.3	38.5
4.59 - 5.91	6.35 $\times 10^{-1}$	$(6.56 \pm 0.05 \pm 0.42) \times 10^1$	8.61×10^1	2.05×10^{-2}	1.75×10^{-2}	2.37×10^{-2}	31.3	27.5	36.7
5.91 - 7.62	8.22 $\times 10^{-1}$	$(4.00 \pm 0.03 \pm 0.25) \times 10^1$	5.11×10^1	1.11×10^{-2}	9.67×10^{-3}	1.27×10^{-2}	27.8	25.0	32.3
7.62 - 9.82	1.06	$(2.33 \pm 0.02 \pm 0.15) \times 10^1$	2.94×10^1	6.13×10^{-3}	5.45×10^{-3}	6.84×10^{-3}	26.3	24.3	30.1
9.82 - 12.7	1.38	$(1.29 \pm 0.01 \pm 0.08) \times 10^1$	1.63×10^1	3.48×10^{-3}	3.17×10^{-3}	3.80×10^{-3}	27.0	25.4	30.1
12.7 - 16.3	1.73	$(7.04 \pm 0.09 \pm 0.44) \times 10^0$	8.90×10^0	1.86×10^{-3}	1.73×10^{-3}	2.00×10^{-3}	26.5	25.4	29.1
16.3 - 21.0	2.26	$(3.78 \pm 0.06 \pm 0.24) \times 10^0$	4.75×10^0	9.74×10^{-4}	9.17×10^{-4}	1.03×10^{-3}	25.8	25.1	28.1
21.0 - 27.1	2.93	$(2.10 \pm 0.04 \pm 0.13) \times 10^0$	2.46×10^0	3.61×10^{-4}	3.37×10^{-4}	3.84×10^{-4}	17.2	17.3	19.4
27.1 - 35.0	3.80	$(1.06 \pm 0.02 \pm 0.07) \times 10^0$	1.26×10^0	2.04×10^{-4}	1.95×10^{-4}	2.14×10^{-4}	19.3	19.6	21.3
35.0 - 45.1	4.86	$(5.34 \pm 0.15 \pm 0.33) \times 10^1$	6.42×10^1	1.08×10^{-4}	1.05×10^{-4}	1.12×10^{-4}	20.3	20.7	22.1
45.1 - 58.2	6.30	$(3.01 \pm 0.10 \pm 0.19) \times 10^1$	3.26×10^1	2.53×10^{-5}	2.39×10^{-5}	2.69×10^{-5}	8.43	10.7	11.4
58.2 - 75.1	8.13	$(1.43 \pm 0.06 \pm 0.09) \times 10^1$	1.63×10^1	1.98×10^{-5}	1.92×10^{-5}	2.04×10^{-5}	13.8	15.4	16.1
75.1 - 96.8	10.4	$(7.49 \pm 0.37 \pm 0.47) \times 10^2$	8.07×10^2	5.83×10^{-6}	5.61×10^{-6}	6.06×10^{-6}	7.79	10.9	11.4
97 - 125	13.5	$(4.22 \pm 0.24 \pm 0.27) \times 10^2$	4.03×10^2	1.89×10^{-6}	1.97×10^6	1.80×10^{-6}	4.47	9.8	9.56
125 - 161	17.3	$(2.03 \pm 0.15 \pm 0.13) \times 10^2$	2.01×10^2	1.97×10^{-7}	2.31×10^{-7}	1.62×10^{-7}	0.969	9.8	9.81
161 - 208	22.6	$(9.85 \pm 0.88 \pm 0.68) \times 10^3$	9.82×10^3	3.41×10^{-8}	4.71×10^{-8}	2.12×10^{-8}	0.347	11.3	11.3

CAPRICE								
Bin (GeV)	η (%)	Data	Model	δ F$_i$	δ F$_{i+}$	δ F$_{i-}$	δ F$_{i}$%	δ F$_{i+}$%	δ F$_{i-}$%
0.15 - 0.23	0.842	$(1.24\pm 0.02)\times10^3$	1.67×10^3	4.28×10^{-1}	4.28×10^{-1}	4.28×10^{-1}	34.5	34.6	34.6
0.23 - 0.33	1.05	$(1.39\pm 0.02)\times10^3$	1.78×10^3	3.90×10^{-1}	3.90×10^{-1}	3.90×10^{-1}	28.1	28.1	28.1
0.33 - 0.47	1.48	$(1.41\pm 0.01)\times10^3$	1.75×10^3	3.45×10^{-1}	3.45×10^{-1}	4.85×10^{-1}	24.5	24.5	24.5
0.47 - 0.62	1.58	$(1.32\pm 0.01)\times10^3$	1.63×10^3	3.15×10^{-1}	3.15×10^{-1}	3.45×10^{-1}	23.8	23.8	23.8
0.62 - 0.78	1.69	$(1.20\pm 0.2)\times10^3$	1.46×10^3	2.62×10^{-1}	2.62×10^{-1}	2.62×10^{-1}	21.8	21.9	21.9
0.78 - 1.12	3.58	$(9.87\pm 0.10)\times10^3$	11.9×10^3	1.98×10^{-1}	1.98×10^{-1}	1.98×10^{-1}	20.1	20.1	20.1
1.12 - 1.48	3.79	$(7.39\pm 0.06)\times10^3$	8.89×10^3	1.50×10^{-1}	1.50×10^{-1}	1.50×10^{-1}	20.3	20.3	20.3
1.48 - 1.85	3.90	$(5.45\pm 0.04)\times10^3$	6.61×10^3	1.16×10^{-1}	1.16×10^{-1}	1.16×10^{-1}	21.4	21.4	21.4
1.85 - 2.23	4.00	$(4.18\pm 0.04)\times10^3$	5.04×10^3	8.57×10^{-2}	8.58×10^{-2}	8.58×10^{-2}	20.5	20.5	20.5
2.23 - 2.61	4.00	$(3.17\pm 0.09)\times10^3$	3.90×10^3	7.26×10^{-2}	7.31×10^{-2}	7.31×10^{-2}	22.9	23.1	23.1
2.61 - 3.00	4.11	$(2.50\pm 0.07)\times10^3$	3.06×10^3	5.56×10^{-2}	5.61×10^{-2}	5.61×10^{-2}	22.3	22.4	22.4
3.00 - 3.39	4.11	$(2.01\pm 0.06)\times10^3$	2.44×10^3	4.33×10^{-2}	4.37×10^{-2}	4.37×10^{-2}	21.6	21.8	21.8
3.39 - 3.84	4.74	$(1.61\pm 0.05)\times10^3$	1.96×10^3	3.55×10^{-2}	3.58×10^{-2}	3.58×10^{-2}	22.0	22.2	22.2
3.84 - 4.40	5.90	$(1.26\pm 0.03)\times10^3$	1.53×10^3	2.70×10^{-2}	2.72×10^{-2}	2.72×10^{-2}	21.4	21.6	21.6
4.40 - 5.13	7.69	$(9.66\pm 0.10)\times10^3$	11.5×10^3	1.84×10^{-2}	1.85×10^{-2}	1.85×10^{-2}	19.1	19.1	19.1
5.13 - 6.10	10.2	$(6.86\pm 0.07)\times10^3$	8.22×10^3	1.36×10^{-2}	1.37×10^{-2}	1.37×10^{-2}	19.9	19.9	19.9
6.10 - 7.46	14.3	$(4.64\pm 0.05)\times10^3$	5.51×10^3	8.74×10^{-3}	8.75×10^{-3}	8.75×10^{-3}	18.8	18.9	18.9
7.46 - 9.49	21.4	$(2.78\pm 0.03)\times10^3$	3.37×10^3	5.85×10^{-3}	5.86×10^{-3}	5.86×10^{-3}	21.1	21.1	21.1

Table 3.3: Comparison between BESS-98, IMAX and CAPRICE data and model's estimates; η represents the weight associated to each energy bin. Discrepancies and relative percentile ratios between data and model estimates are also reported. Unit of measures for fluxes is c s^{-1} m^{-2} sr^{-1} MeV^{-1}.

LEO and balloon-borne missions' resume				
	AMS-01	BESS-98	IMAX	CAPRICE
Type	Spaceborne	Balloon-borne	Balloon-borne	Balloon-borne
Period	June 1998	July 1998	July 1992	August 1994
Altitude (km)	380 ($\sim 51.7°$)	37	36	36 - 38.1
Geomag. lat. (°)	0-$\sim$63	$\sim$65.3	$\sim$65.3	$\sim$65.3
ϕ (MV)	650	650	750 ± 50	$\sim$600

Table 3.4: A resume of the AMS-01, BESS, IMAX and CAPRICE mission parameters

Appendix C

Results for XRISM

Year	g_1^0 (nT)
2020	29275.4 ± 50.2
2025	29184.25 ± 50.2
2030	29093.1 ± 50.2
2035	29001.95 ± 50.2
2040	28910.8 ± 50.2
2045	28819.65 ± 50.2

Table 4.1: G_0^1 forecast for the 2020-2045 years' range.
The uncertainty has been obtained by performing the mean value among the discrepancies between the official values and the best fit straight line's estimates.

XRISM's results - worst scenario				
Average energy (GeV)	Energy's uncertainty (GeV)	XRISM's estimated flux	AMS-01's uncertainty (%)	XRISM's flux uncertainty
6.155	0.705	5.4×10^{-5}	132	7.14×10^{-5}
7.73	0.87	3.14×10^{-4}	107	3.35×10^{-4}
9.665	1.065	1.75×10^{-3}	98.5	1.72×10^{-3}
12.035	1.305	6.26×10^{-3}	57.2	3.58×10^{-3}
14.945	1.605	7.28×10^{-3}	11.2	8.14×10^{-4}
18.515	1.965	4.66×10^{-3}	3.94	1.84×10^{-4}
22.885	2.405	2.72×10^{-3}	3.76	1.02×10^{-4}
28.245	2.955	1.56×10^{-3}	3.84	6.00×10^{-5}
34.815	3.615	8.93×10^{-4}	4.65	4.15×10^{-5}
42.865	4.435	5.09×10^{-4}	4.37	2.22×10^{-5}
52.73	5.43	2.90×10^{-4}	5.92	1.72×10^{-5}
64.82	6.66	1.65×10^{-4}	5.39	8.86×10^{-6}
79.635	8.155	9.33×10^{-5}	4.21	3.92×10^{-6}
97.785	9.995	5.28×10^{-5}	5.52	2.91×10^{-6}
120.025	12.245	2.99×10^{-5}	10.4	3.11×10^{-6}
147.28	15.01	1.69×10^{-5}	10.7	1.81×10^{-6}
180.675	18.385	9.52×10^{-6}	5.37	5.11×10^{-7}

Table 4.2: Results for the XRISM's estimated primary protons assuming the worst scenario approach.

XRISM's results - realistic scenario				
XRISM's estimated flux	AMS-01's top uncertainty (%)	AMS-01's bottom uncertainty (%)	XRISM's top uncertainty	XRISM's bottom uncertainty
5.4×10^{-5}	132	81.1	7.14×10^{-5}	4.38×10^{-5}
3.14×10^{-4}	107	25.0	3.35×10^{-4}	7.84×10^{-5}
1.75×10^{-3}	98.5	22.0	1.72×10^{-3}	3.84×10^{-4}
6.26×10^{-3}	57.2	16.7	3.58×10^{-3}	1.04×10^{-3}
7.28×10^{-3}	11.2	5.84	8.14×10^{-4}	4.25×10^{-4}
4.66×10^{-3}	3.94	3.82	1.84×10^{-4}	1.78×10^{-4}
2.72×10^{-3}	3.76	3.76	1.02×10^{-4}	1.02×10^{-4}
1.56×10^{-3}	3.84	3.84	6.00×10^{-5}	6.00×10^{-5}
8.93×10^{-4}	4.65	4.65	4.15×10^{-5}	4.15×10^{-5}
5.09×10^{-4}	4.37	4.37	2.22×10^{-5}	2.22×10^{-5}
2.90×10^{-4}	5.92	5.92	1.72×10^{-5}	1.72×10^{-5}
1.65×10^{-4}	5.39	5.39	8.86×10^{-6}	8.86×10^{-6}
9.33×10^{-5}	4.21	4.21	3.92×10^{-6}	3.92×10^{-6}
5.28×10^{-5}	5.52	5.52	2.91×10^{-6}	2.91×10^{-6}
2.99×10^{-5}	10.4	10.4	3.11×10^{-6}	3.11×10^{-6}
1.69×10^{-5}	10.7	10.7	1.81×10^{-6}	1.81×10^{-6}
9.52×10^{-6}	5.37	5.37	5.11×10^{-7}	5.11×10^{-7}

Table 4.3: Results for the XRISM's estimated primary protons assuming the realistic approach.

XRISM's results - middle ground		
XRISM's estimated flux	AMS-01's average uncertainty	XRISM's uncertainty
5.4×10^{-5}	107	5.76×10^{-5}
3.14×10^{-4}	65.8	2.06×10^{-4}
1.75×10^{-3}	60.2	1.05×10^{-3}
6.26×10^{-3}	36.9	2.31×10^{-3}
7.28×10^{-3}	8.51	6.19×10^{-4}
4.66×10^{-3}	3.88	1.81×10^{-4}
2.72×10^{-3}	3.76	1.02×10^{-4}
1.56×10^{-3}	3.84	6.00×10^{-5}
8.93×10^{-4}	4.65	4.15×10^{-5}
5.09×10^{-4}	4.37	2.22×10^{-5}
2.90×10^{-4}	5.92	1.72×10^{-5}
1.65×10^{-4}	5.39	8.86×10^{-6}
9.33×10^{-5}	4.21	3.92×10^{-6}
5.28×10^{-5}	5.52	2.91×10^{-6}
2.99×10^{-5}	10.4	3.11×10^{-6}
1.69×10^{-5}	10.7	1.81×10^{-6}
9.52×10^{-6}	5.37	5.11×10^{-7}

Table 4.4: Results for the XRISM's estimated primary protons assuming the middle ground approach.

Bibliography

[1] M Ajello, D Gasparrini, Miguel Sánchez-Conde, G Zaharijas, M Gustafsson, J Cohen-Tanugi, CD Dermer, Yoshiyuki Inoue, D Hartmann, M Ackermann, et al. The origin of the extragalactic gamma-ray background and implications for dark matter annihilation. *The Astrophysical Journal Letters*, 800(2):L27, 2015.

[2] Gang Bao, Wei-Tou Ni, DNA Shaul, HM Araujo, Lei Liu, and TJ Sumner. Improved simulation of the mass charging for astrod i. *arXiv preprint arXiv:0707.1930*, 2007.

[3] V Fioretti, A Bulgarelli, G Malaguti, V Bianchin, M Trifoglio, and F Gianotti. The low earth orbit radiation environment and its impact on the prompt background of hard x-ray focusing telescopes. In *High Energy, Optical, and Infrared Detectors for Astronomy V*, volume 8453, page 845331. International Society for Optics and Photonics, 2012.

[4] Ilya G Usoskin, Galina A Bazilevskaya, and Gennady A Kovaltsov. Solar modulation parameter for cosmic rays since 1936 reconstructed from ground-based neutron monitors and ionization chambers. *Journal of Geophysical Research: Space Physics*, 116(A2), 2011.

[5] DF Smart and MA Shea. A review of geomagnetic cutoff rigidities for earth-orbiting spacecraft. *Advances in Space Research*, 36(10):2012–2020, 2005.

[6] J Nevalainen, IG Usoskin, and A Mishev. Eccentric dipole approximation of the geomagnetic field: application to cosmic ray computations. *Advances in Space Research*, 52(1):22–29, 2013.

[7] P Cumani, M Hernanz, J Kiener, V Tatischeff, and A Zoglauer. Background for a gamma-ray satellite on a low-earth orbit. *Experimental Astronomy*, 47(3):273–302, 2019.

[8] Hertz, paul (22 june 2017). "astrophysics" (pdf). nasa. retrieved 2017-07-01. `https://www.nsf.gov/attachments/190966/public/HertzAAAC2017Jun22FINAL2.pdf`.

[9] https://www.isas.jaxa.jp/en/missions/spacecraft/developing/xrism.html. `https://www.isas.jaxa.jp/en/missions/spacecraft/developing/xrism.html`.

[10] Erwan Thébault, Christopher C Finlay, Ciarán D Beggan, Patrick Alken, Julien Aubert, Olivier Barrois, Francois Bertrand, Tatiana Bondar, Axel Boness, Laura Brocco, et al. International geomagnetic reference field: the 12th generation. *Earth, Planets and Space*, 67(1):79, 2015.

[11] https://www.lescienze.it/news/2019/08/26/news/inversione$_c ampo_m agnetico_t erra_d urata - 4518304/ : : $text = in$

Ringraziamenti

Ringrazio il Professore Gabriele Giovannini per i molti preziosi consigli che mi ha dato e per avermi fatto da relatore per questa tesi e la Dott.ssa Valentina Fioretti per avermi seguito sia durante la stesura della stessa sia durante il tirocinio svolto presso l'INAF OAS di Bologna.

Dedico questa tesi:
Alla mia famiglia, per esserci sempre stata e per avermi permesso di intraprendere e portare a termine questo percorso.
Alla memoria di Swami Sri Yukteswarji, Paramhansa Yoganandaji e Tiziano Terzani, e a Dante, che mi hanno aiutato a trovare la mia strada.
A Valentina, che mi é stata sempre vicino motivandomi ad ogni esame.
Al mio collega e amico Corrado, assieme al quale ho percorso gran parte di questa avventura.
Alla memoria del mio amato cugino Filippo, con il quale tanto avrei condiviso di ció cose che studio.
A me stesso, che ho trovato la forza per mettermi in gioco ed aprire, dopo 25 anni, il primo libro di matematica, e la determinazione per apprendere e amare ció che per un quarto di secolo ho pensato non avrei mai appreso e amato.